







# Ultrafast longitudinal imaging of haemodynamics via single-shot volumetric photoacoustic tomography with a single-element detector

Received: 15 March 2023

Accepted: 25 October 2023

Published online: 30 November 2023

 Check for updates

Yide Zhang <sup>1,4</sup>, Peng Hu <sup>1,4</sup>, Lei Li<sup>1</sup>, Rui Cao <sup>1</sup>, Anjul Khadria <sup>1</sup>, Konstantin Maslov<sup>1</sup>, Xin Tong<sup>1</sup>, Yushun Zeng <sup>2,3</sup>, Laiming Jiang <sup>2,3</sup>, Qifa Zhou <sup>2,3</sup> & Lihong V. Wang <sup>1</sup> 

Techniques for imaging haemodynamics use ionizing radiation or contrast agents or are limited by imaging depth (within approximately 1 mm), complex and expensive data-acquisition systems, or low imaging speeds, system complexity or cost. Here we show that ultrafast volumetric photoacoustic imaging of haemodynamics in the human body at up to 1 kHz can be achieved using a single laser pulse and a single element functioning as 6,400 virtual detectors. The technique, which does not require recalibration for different objects or during long-term operation, enables the longitudinal volumetric imaging of haemodynamics in vasculature a few millimetres below the skin's surface. We demonstrate this technique in vessels in the feet of healthy human volunteers by capturing haemodynamic changes in response to vascular occlusion. Single-shot volumetric photoacoustic imaging using a single-element detector may facilitate the early detection and monitoring of peripheral vascular diseases and may be advantageous for use in biometrics and point-of-care testing.

Vascular diseases, such as atherosclerosis, thrombosis, aneurysms and peripheral vascular diseases, pose serious health risks such as heart attack, stroke, organ failure and complications in the lower extremities, particularly in patients with diabetes<sup>1,2</sup>. The importance of early detection and intervention in these diseases through imaging of haemodynamics, especially in the monitoring of the blood supply to lower extremities, cannot be overstated, given that it paves the way for timely treatment and reduces the risk of severe outcomes such as amputations<sup>3,4</sup>. The efficacy of pharmacological therapies and surgical interventions can be evaluated by monitoring changes in haemodynamics<sup>5</sup>. Moreover, measuring factors such as blood-flow velocity

can also assess an individual's risk of developing vascular diseases, aiding preventive measures and facilitating personalized treatment plans. Overall, imaging of haemodynamics has a vital role in disease diagnosis, treatment, prevention and research, especially in managing diseases that affect the lower extremities, ultimately improving patient outcomes and advancing medical research<sup>1</sup>.

There are several techniques available to image haemodynamics in the human body, each with its own strengths and limitations. Magnetic resonance imaging, computed tomography angiography and positron emission tomography all have the ability to produce high-resolution images of the vascular system and blood-flow dynamics, but they

<sup>1</sup>Caltech Optical Imaging Laboratory, Andrew and Peggy Cherg Department of Medical Engineering, Department of Electrical Engineering, California Institute of Technology, Pasadena, CA, USA. <sup>2</sup>USC Roski Eye Institute, University of Southern California, Los Angeles, CA, USA. <sup>3</sup>Alfred E. Mann Department of Biomedical Engineering, University of Southern California, Los Angeles, CA, USA. <sup>4</sup>These authors contributed equally: Yide Zhang, Peng Hu.

 e-mail: [LVW@caltech.edu](mailto:LVW@caltech.edu)

require the use of ionizing radiation and the injection of contrast agents, which can have adverse health effects<sup>6–8</sup>. Moreover, relying on strong ionizing sources and numerous detector elements, these techniques are bulky and expensive, making them inaccessible to mobile clinics or small healthcare facilities. Optical imaging techniques, such as fluorescence imaging and optical coherence tomography, offer non-invasive visualization of haemodynamics, but their penetration depths are constrained by the optical diffusion limit (around 1–2 mm) and do not have sufficient specificity to haemoglobin<sup>9,10</sup>. Doppler ultrasound is another option, providing real-time measurement of blood flow velocity and direction. However, even with recent improvements in minimizing ultrasound probes, state-of-the-art ultrasound imaging techniques still require burdensome and costly data acquisition systems, such as Verasonics, due to hundreds to thousands of detector elements<sup>11,12</sup>.

Photoacoustic tomography (PAT), also known as optoacoustic tomography, offers a promising solution to the limitations faced by other imaging techniques for haemodynamic imaging<sup>13–15</sup>. In contrast to other techniques, PAT uses the photoacoustic (PA) effect to absorb the energy of incident photons by optical absorbers, such as haemoglobin, in biological tissue and re-emit them as ultrasonic waves (PA waves) to generate optical contrast tomographic images<sup>16–19</sup>. As a result, PAT does not rely on ionizing radiation or contrast agents. Moreover, owing to the weak scattering of ultrasound in biological tissue, PAT provides a depth-to-resolution ratio of approximately 200, enabling high spatial resolution at depths up to several centimetres<sup>13</sup>. Two primary forms of PAT are photoacoustic microscopy<sup>19–21</sup>, which requires sequential scanning of the probing beam, and photoacoustic computed tomography (PACT)<sup>17,22,23</sup>, which captures a three-dimensional (3D) image using one or a few pulses of the probing beam. Photoacoustic microscopy uses a single-element detector, which requires a simple data-acquisition system but has a low imaging speed. By contrast, although PACT can offer higher imaging speeds of up to kilohertz<sup>24,25</sup>, it necessitates a number of detection elements and corresponding data acquisition systems. This results in a system that is complex, costly and bulky.

To overcome the challenges of complexity, cost and size in PACT systems, researchers have been working on ways to reduce the number of detector elements that are needed to reconstruct a 3D image. One promising approach uses the principles of compressive sensing and single-pixel imaging<sup>26–29</sup>, which use acoustic scatterers to achieve PA or ultrasound tomography with just a single detector element<sup>30–33</sup>. However, these techniques are time consuming, as they require a sequence of measurements with different mask configurations, limiting their speed. To address this issue, researchers have developed methods that take advantage of the spatiotemporal encoding of an ergodic relay (ER) or a chaotic cavity<sup>34,35</sup>. These techniques can produce single-shot images while using fewer detector elements<sup>36–40</sup>. However, they have been demonstrated only for two-dimensional (2D) imaging and require recalibration for different objects, which can be time consuming. Moreover, they may not be suitable for long-term imaging in unstable environments owing to their sensitivity to boundary conditions. Recently, our group developed a spatiotemporal encoder that enables single-shot 2D imaging of thin objects, such as thin black rubber, using a single-element detector without the need of object-specific calibration<sup>41</sup>. However, owing to contamination from signals outside of the calibration plane, this approach cannot provide volumetric imaging of thicker 3D objects such as blood vessels *in vivo*. Moreover, as the spatiotemporal encoder and the transducer are not integrated, the system is susceptible to mechanical vibrations and thermal fluctuations. This necessitates periodic recalibration, therefore making the system unsuitable for long-term imaging in unstable environments.

In this Article, we present PACT through an ER (PACTER), a PACT system that simultaneously addresses the challenges faced by previous imaging techniques. PACTER provides a highly accessible and efficient

solution, paving the way for non-invasive, label-free and ultrafast volumetric imaging of haemodynamics at depth in humans. With PACTER, a single-element detector encodes information equivalent to that of 6,400 virtual detectors, enabling the reconstruction of a tomographic image of vasculature in 3D with just a single laser pulse. The system achieves longitudinal volumetric imaging at kilohertz rates, making it possible to capture fast haemodynamics in the human body in real-time. We demonstrate PACTER's ability in monitoring vital signs in small animals and in visualizing human haemodynamics in response to cuffing, capturing the variability in blood flow speeds. We also show that PACTER can capture the haemodynamic changes in human foot vessels during vascular occlusion, demonstrating its potential as a powerful tool for assessing vascular function in the lower extremities. Enabled by the integrated ultrasonic transducer and the object-independent universal calibration, the system needs to be calibrated only once and is suitable for long-term imaging in unstable environments. PACTER's single-element detector design makes it convenient, affordable and compact, and is therefore translatable to clinical applications such as home-care monitoring<sup>42,43</sup>, biometrics, point-of-care testing<sup>44</sup> and non-invasive haemodynamic monitoring in intensive care units<sup>45</sup>. PACTER's ability to capture dynamic changes in vascular occlusion presents clinical potential for early detection, enhanced assessment and more personalized treatment of peripheral vascular diseases. The single-element detector concept in PACTER can also be generalized to other imaging technologies, such as ultrasonography<sup>46</sup>, sonar<sup>47</sup> and radar<sup>48</sup>.

## Results

### PACTER system

The PACTER system requires calibration only once before its use for a complete series of imaging (Methods). In the calibration procedure (Fig. 1a), the laser beam was transmitted through the ER and focused onto a uniform optical absorber placed on top of the ER. We chose lysed bovine blood as our calibration target because our primary imaging objects are blood vessels, making bovine blood a relevant standard. Moreover, our experiments demonstrated that bovine blood provides more-stable PACTER signals compared with other uniform absorbers, such as black tape, black rubber and black ink, which are more susceptible to photobleaching (Supplementary Fig. 1). One reason for the stability of blood is its fluid nature. If we bleach it, the movement can replenish the bleached portion, making it more stable than solid substances such as black tape or black rubber. Moreover, the pigment in black ink absorbs 532 nm light more intensely than the haemoglobin in the blood, making it more vulnerable to photobleaching<sup>49</sup>. Using two motorized stages, we controlled the positions of a pair of mirrors to steer the focused laser beam across the field of view (FOV) in the *x–y* plane and recorded the PACTER signals at each scanning position. After calibration, the uniform optical absorber could be removed, and the system was ready for imaging. In the imaging procedure (Fig. 1b), the focusing lens was replaced by a fly's eye homogenizer (Supplementary Fig. 2), which converted the incident laser beam into a wide-field, homogenized illumination pattern that had the same shape and width as that of the calibration FOV (Supplementary Note 1). Note that the illumination pattern does not necessarily have to be identical to the calibration FOV (Supplementary Fig. 3). To acquire imaging data, the object was directly placed on top of the ER using ultrasound gel as the coupling medium, and we recorded the PACTER signal generated by the object after each laser pulse.

To enhance the detection sensitivity and improve the stability of the system for long-term *in vivo* imaging in unstable environments, we fabricated a single-element ultrasonic transducer integrated onto the hypotenuse surface of the prism of the ER (Fig. 1c), whereby the transducer does not interact with the illumination laser beam (Supplementary Fig. 4). The transducer was based on a lead magnesium niobate–lead titanate (PMN-PT) single crystal (Supplementary Figs. 5

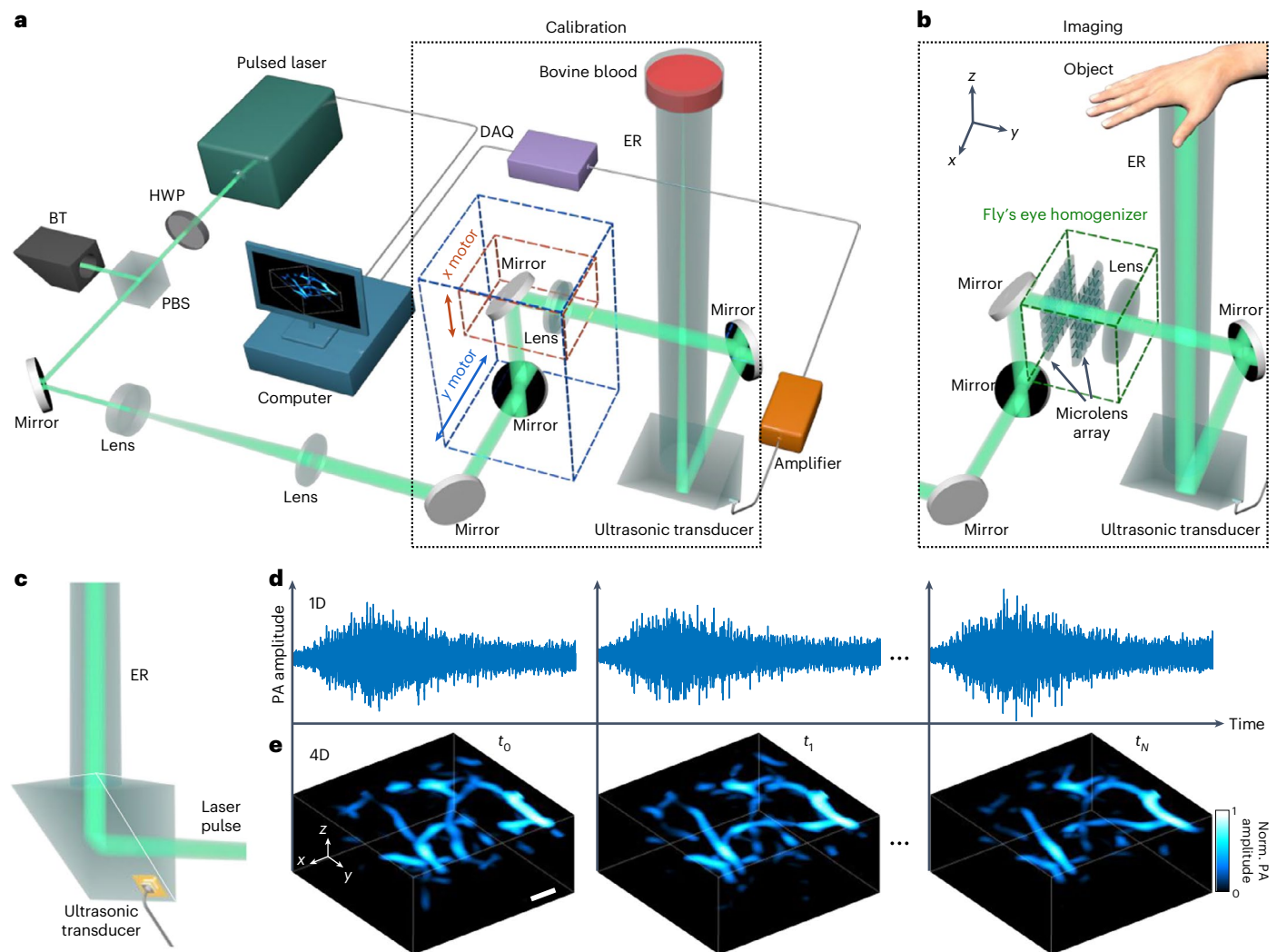


**Fig. 1 | The PACTER system. a, b.** Schematic of the PACTER system calibration (a) and imaging (b) procedures. BT, beam trap; DAQ, data acquisition unit; HWP, half-wave plate; PBS, polarizing beam splitter; ER, ergodic relay. The differences between the two modes are highlighted by the black dotted boxes. c, Schematic

of the single-element ultrasonic transducer fabricated on the ER. d, 1D  $(t)$  PACTER signals detected by the ultrasonic transducer at time instances  $t_0$ ,  $t_1$  and  $t_N$ . e, Reconstruction of a 4D  $(xyzt)$  image of human palmar vessels from the signals in d. Norm., normalized. Scale bar, 1 mm.

and 6), which achieved exceptional piezoelectric performance, such as a high piezoelectric constant ( $d_{33}$ ) and electromechanical coupling coefficient ( $k_t$ )<sup>50–52</sup>. Compared with a post-fabrication transducer that is coupled to the ER with resin, the integrated PMN-PT transducer achieved greater sensitivity over a broad band (Supplementary Fig. 7). Furthermore, as one of the gold electrodes of the transducer was directly sputtered onto the surface of the ER (Methods), the PACTER signals inside the ER could reach the transducer with the maximum transmission, and the transducer and the ER became an integrated piece that facilitated stable data acquisition for long-term in vivo imaging in unstable environments.

Conventionally, a single-element ultrasonic transducer can acquire only a one-dimensional (1D) signal in the time domain (Fig. 1d). However, with the ER, PACTER can use the single-element transducer to encode spatiotemporal information equivalent to those captured by 6,400 detectors (Supplementary Video 1), which can then be used to reconstruct a 3D map of the optical absorbers in the imaging volume. With a kilohertz laser repetition rate, PACTER can use the 1D  $(t)$  signals to generate a thousand 3D  $(xyz)$  volumes per second, leading to a high-speed four-dimensional (4D)  $(xyzt)$  image of optical absorption in, for example, human palmar vessels (Fig. 1e).

### PACTER signal and reconstruction

PACTER needs only a one-time universal calibration despite its more stringent requirement for 3D imaging (Supplementary Note 2, Supplementary Fig. 8 and Supplementary Video 2). In our experiments, we found that calibration data acquired over the course of a year could all be used for reconstruction (Supplementary Fig. 9). This suggests that a single calibration dataset could be effective for at least a year. In the calibration procedure, the focused laser beam was scanned across the FOV in 80 by 80 steps with a step size of 0.1 mm (Fig. 2a). To ensure that the PACTER signal acquired at each calibration pixel was distinct from others, we chose a step size of about a half of the full width at half maximum of a line profile along the cross-correlation map, that is, about 0.21 mm (Supplementary Fig. 10). Although the calibration signals were obtained by scanning the laser beam across a 2D plane, they could be used as  $80 \times 80 = 6,400$  virtual transducers for 3D reconstruction (Fig. 2b) because (1) the PACTER signals were object-independent; and (2) the calibration signals were generated at the bottom of the 3D imaging volume. When source points in the 3D volume ( $\mathbf{r}'_m, m = 1, 2, \dots$ ) were illuminated by a laser pulse, the PA signals that they generated would propagate to the calibrated virtual transducers ( $\mathbf{r}_n, n = 1, 2, \dots$ ) after time  $t_{m,n} = \|\mathbf{r}'_m - \mathbf{r}_n\|/c$ , where  $c$  is the speed of the sound in the



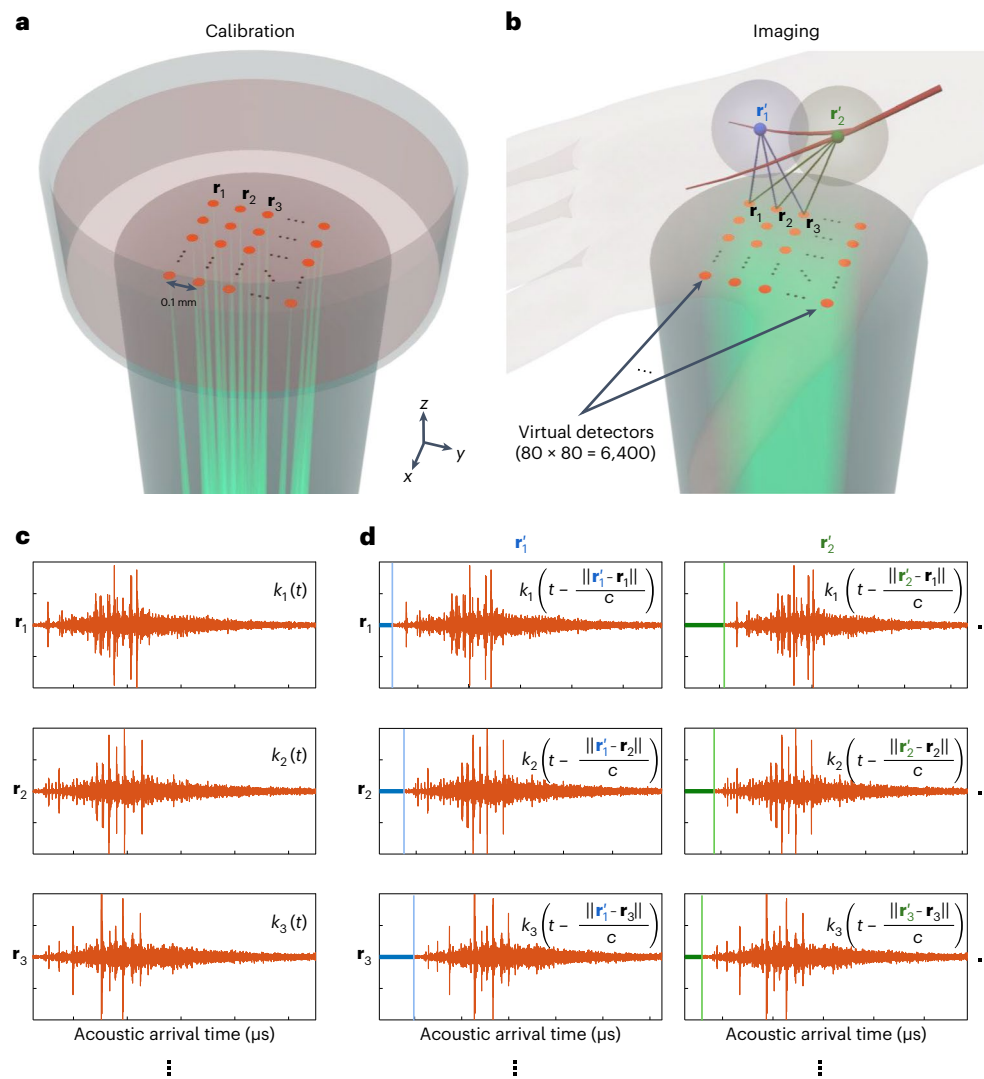


**Fig. 2 | Single-shot 3D reconstruction in PACTER.** **a**, Illustration of the calibration procedure of PACTER. Focused laser beams for calibration are shown in green. Calibration pixels are highlighted as orange dots. The calibration step size is 0.1 mm. The calibration pixels ( $80 \times 80$ ) become 6,400 virtual transducers.  $\mathbf{r}_1$ ,  $\mathbf{r}_2$  and  $\mathbf{r}_3$  are the positions of three calibrated virtual transducers. **b**, Illustration of PACTER of human palmar vessels. The homogenized beam for wide-field illumination is shown in green.  $\mathbf{r}'_1$  and  $\mathbf{r}'_2$  are the positions of two source points in the vessels. The blue and green spheres denote the PA waves generated by the

source points. The calibrated virtual transducers capture the PA signals from  $\mathbf{r}'_1$  and  $\mathbf{r}'_2$  with different delays, indicated by the thick blue and green lines. **c**, The PACTER signals  $k_1(t)$ ,  $k_2(t)$ ,  $k_3(t)$  of the calibrated virtual transducers corresponding to  $\mathbf{r}_1$ ,  $\mathbf{r}_2$ ,  $\mathbf{r}_3$ , respectively. **d**, The PACTER signal from the wide-field imaging consists of PA signals from  $\mathbf{r}'_1$  and  $\mathbf{r}'_2$ , which are essentially  $k_1(t)$ ,  $k_2(t)$ ,  $k_3(t)$  delayed according to the distance between the calibrated virtual transducer and the source point.

medium. Then, these signals would follow the same acoustic path inside the ER to the ultrasonic transducer as that of the calibration signals. From the transducer's perspective, compared with the calibration signal  $k_n(t)$  acquired at  $\mathbf{r}_n$  (Fig. 2c), the signal from the source point  $\mathbf{r}'_m$  relayed through  $\mathbf{r}_n$  is proportional to  $k_n(t)$  delayed by  $t_{m,n}$ , that is,  $k_n(t - \|\mathbf{r}'_m - \mathbf{r}_n\|/c)$  (Fig. 2d). The signal is modulated by both  $p_{0,m}$ , the initial pressure at  $\mathbf{r}'_m$ , and a weighting factor dependent on the angle and distance. Accordingly, we developed an algorithm to reconstruct the initial pressure in the 3D volume (Methods). Owing to the prohibitively computationally intensive nature of the reconstruction, we reformulated the forward model through temporal convolution and implemented it using fast Fourier transformation. Numerical simulations reveal that this approach increased the computational efficiency by  $9,100\times$  (Supplementary Note 3).

### Spatiotemporal characterization of PACTER

Using the signals acquired by the single detector, PACTER can image the 3D structure of a curved black wire with a single laser pulse

(Fig. 3a) and the 4D dynamics of bovine blood flushing through an S-shaped tube when the tube was illuminated by multiple laser pulses (Fig. 3b and Supplementary Video 3). To evaluate whether the 3D volumes reconstructed by PACTER were correct measurements of the objects, we first compared the perspective views of the 3D volumes reconstructed by PACTER with the ground-truth projection images formed by raster-scanning the laser beam across the objects (Supplementary Fig. 11). Despite a lower spatial resolution compared with the ground truth, the comparison demonstrates that PACTER can correctly reconstruct the 3D objects in the lateral ( $x$ - $y$ ) directions. However, it is important to note that, in the case of in vivo mouse abdominal vasculature, the higher fluence of the focused laser beam compared with the wide-field homogenized beam enabled the ground-truth projection image (Supplementary Fig. 11d) to reveal deeper blood vessels. These vessels were not visible in the PACTER image (Supplementary Fig. 11h). Second, we imaged a thin object in water, of which the  $z$  positions were precisely controlled and measured using a linear translation stage. We imaged the object at multiple  $z$  positions, reconstructed the 3D

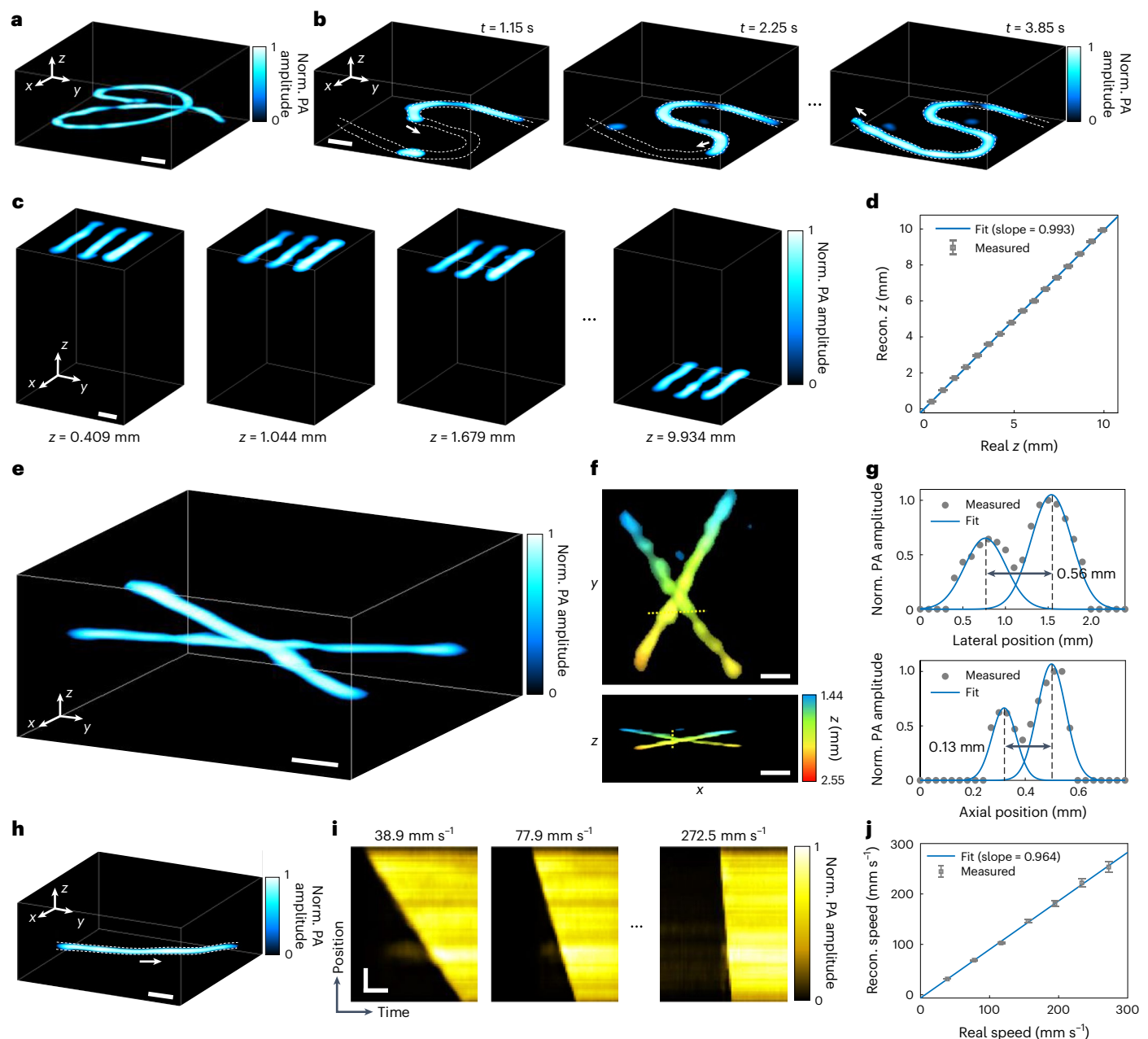


**Fig. 3 | Spatiotemporal characterization of PACTER. a**, 3D PACTER image of a curved black wire. **b**, Images of 4D PACTER showing bovine blood flushing through an S-shaped tube. **c**, 3D PACTER images of three bars printed with black ink onto a transparent film. In each image, the object was placed at a different  $z$  position. **d**, Reconstructed (recon.) versus real  $z$  positions of the objects in **c**. Data are mean  $\pm$  s.e.m.  $n = 1,980$ . The blue curve represents a linear fit. **e**, 3D PACTER image of two crossing human hairs in agarose. **f**, Maximum  $z$ -projections (top) and  $y$ -projections (bottom) of the 3D volume in **e**. The  $z$  positions of the object are colour coded. **g**, Profiles along the yellow dotted lines in **f** denoted by

grey dots. The blue curves represent two-term Gaussian fits. The black arrows denote the minimum distances that can separate the two hairs. **h**, 3D PACTER image of bovine blood flushing through a tube. The white arrow indicates the flushing direction. **i**, PA amplitudes along the tube in **h** over time, when the blood flushes through the tube at different speeds. Scale bars, 1 mm (vertical) and 50 ms (horizontal). **j**, The speeds of the blood flow were quantified from the reconstructed images versus the real speeds in **i**. Data are mean  $\pm$  s.e.m.  $n = 74$ . The blue curve represents a linear fit. For **a–c**, **e**, **f** and **h**, scale bar, 1 mm.

volumes (Fig. 3c) and compared the  $z$  positions in the reconstructed volumes with the real ones. As shown in Fig. 3d, the reconstructed and real  $z$  positions were linearly related ( $R^2 = 1.000$ ) with a slope (0.993) close to 1, demonstrating that PACTER can accurately reconstruct the 3D objects in the axial ( $z$ ) direction.

To quantify the resolution of PACTER, we imaged two human hairs embedded in an agarose block (Fig. 3e). The hairs were intentionally positioned such that they were in close contact with each other, forming a crossing pattern that could be seen in both  $z$ - and  $y$ -projections

(Fig. 3f). Defining the spatial resolution as the minimum distance that can distinguish the peaks of the two hairs, we found the lateral and axial resolutions of PACTER to be 0.56 mm and 0.13 mm, respectively (Fig. 3g). The anisotropic spatial resolutions along the lateral and axial directions were related to the image-formation process in PACTER (Supplementary Notes 4 and 5 and Supplementary Figs. 12 and 13). The coarser lateral resolution was due to the acoustic impedance mismatch between the object and the ER, which led to a limited-view effect that reduced coupling for propagation directions beyond the

critical angle of the ultrasonic wave's refraction from water into fused silica (Supplementary Note 4), while both resolutions were limited by the frequency-dependent acoustic attenuation (Supplementary Fig. 14). By imaging a thin object placed at different  $z$  positions, we found that the resolution of PACTER was not sensitive to the imaging depth (Supplementary Fig. 15).

To evaluate whether PACTER could be reliably used to image 4D dynamics, that is, time-lapse movements of 3D objects, we captured 4D images of bovine blood flushing through a tube at different speeds precisely controlled by a syringe pump (Fig. 3h and Supplementary Video 4). On the basis of the reconstructed 4D images, we plotted the PA amplitudes along the tube (ID images) over time (Fig. 3i), calculated the speeds of the blood flow (Supplementary Fig. 16) and compared them with the real speeds set by the syringe pump (Fig. 3j). A linear relationship ( $R^2 = 0.999$ ) between the reconstructed and real speeds with a slope (0.964) close to 1 can be observed, demonstrating that PACTER is capable of 4D imaging, faithfully reconstructing the dynamics of 3D objects over time. Empowered by the imaging speed of up to a thousand volumes per second, PACTER could resolve the high-speed dynamics of the blood flushing through the tube at  $272.5 \text{ mm s}^{-1}$  in 3D, with a temporal resolution of 1 ms (Supplementary Video 5).

#### 4D in vivo imaging of mouse haemodynamics with PACTER

Enabled by its ability of non-invasive, label-free and ultrafast 3D imaging, PACTER is expected to be suitable for monitoring haemodynamics in vivo. Here we evaluated PACTER's ability in monitoring vital signs in small animals. We imaged the haemodynamics of the abdominal regions of mice (Fig. 4a). With a single laser pulse, PACTER could reconstruct the abdominal vasculature in 3D (Fig. 4b,c). When multiple laser pulses were used, PACTER revealed the 4D dynamics of the blood vessels (Supplementary Videos 6 and 7). On the basis of the 4D PACTER datasets, we isolated individual blood vessels from the cross sections of the 3D volumes (Fig. 4d,e) and visualized their motions and structural changes (Fig. 4f,g).

By recording the time-lapse changes of the centre positions and widths of the blood vessels, the respiratory motion could be tracked and identified (Fig. 4h,i). Using Fourier analysis, we found that the centre position of the blood vessel of mouse 1 fluctuated periodically, exhibiting a respiratory frequency of 1.8 Hz (Fig. 4j), whereas the width of the vessel was relatively stable. By contrast, a respiratory frequency of 1.4 Hz could be observed on the basis of both the centre position and the width of the blood vessel of mouse 2 (Fig. 4k). Moreover, when we imaged the third mouse (Supplementary Video 8), we observed a respiratory frequency of 1.9 Hz from the width, not the centre position, of the blood vessel (Extended Data Fig. 1). The distinct 4D haemodynamics of the blood vessels from the three mice demonstrated that PACTER could be a practical tool in monitoring vital signs, such as breathing, in small animals. Note that we did not observe heartbeats, as our imaging was focused on the abdominal region of the mouse, which is distant from the thoracic region<sup>17</sup>, and our system's sensitivity was insufficient to detect the PA signal changes within the pulsating arteries.

#### 4D in vivo imaging of haemodynamics in human hands using PACTER

To demonstrate PACTER's effectiveness in monitoring haemodynamics in humans, we imaged the hand vasculature of two participants. Different regions of the hand, such as the fingers, proximal phalanx and thenar regions, were imaged independently as the participants moved their hands to align those regions with the ER (Extended Data Fig. 2). In the following study, we focused on imaging the participants' thenar vasculature and their responses to cuffing, which was induced by a sphygmomanometer wrapped around the participants' upper arm (Fig. 5a). Using PACTER, we imaged the thenar vasculature in 3D with single laser pulses (Fig. 5b,c) and reconstructed the 4D dynamics of the blood vessels in response to cuffing (Supplementary Videos 9 and 10).

As shown in the maximum-amplitude projections of the 4D datasets (Fig. 5d,e), whereas some blood vessels exhibited a non-decreased PA amplitude throughout the experiment, the other vessels showed a decreased PA amplitude after cuffing due to the occlusion of blood flows; when the cuffing was released, the blood flows recovered, and the PA amplitude was rapidly restored (Fig. 5f,g). The different haemodynamics of these two types of blood vessel in response to cuffing indicate their distinct roles in the circulatory system<sup>53</sup>: the blood vessels with non-decreased and decreased PA amplitudes could be venous and arterial, respectively, agreeing with the observations reported in other cuffing-based studies<sup>54–56</sup>. With the ability to simultaneously image both arterial and venous blood in vivo, PACTER provides additional benefits over conventional pulse oximetry, which can monitor only arterial blood without spatial resolution<sup>57</sup>.

As PA amplitudes have 100% sensitivity to optical absorption<sup>13</sup>, the 4D haemodynamics imaged by PACTER revealed the real-time changes in the blood vessels in response to cuffing, and the linear position of the blood front during the recovery phase could be used to measure the blood flow speed<sup>56</sup>. For participant 1, the occlusion rate of the vessel was found to be  $1.3 \pm 0.1 \text{ m s}^{-1}$ , significantly slower than the blood flow speed of  $16.1 \pm 3.1 \text{ m s}^{-1}$  extracted from the recovery phase (Fig. 5h,i). For participant 2, the occlusion rate and the blood flow speed of the vessel were found to be  $2.4 \pm 0.2 \text{ m s}^{-1}$  and  $26.3 \pm 6.4 \text{ m s}^{-1}$ , respectively (Fig. 5j,k), exhibiting a greater blood flow speed compared with participant 1 (Fig. 5l). Immediately after an imaging session, we asked participant 1 to slightly move their hand and used PACTER to image a different area of the thenar region (Supplementary Video 11). Using the same analysis on a different blood vessel, the occlusion rate and the blood flow speed were found to be  $0.6 \pm 0.1 \text{ m s}^{-1}$  and  $21.6 \pm 7.9 \text{ m s}^{-1}$ , respectively (Extended Data Fig. 3). Taken together, we demonstrated that PACTER could monitor haemodynamics in humans, including the consistent responses of thenar vasculature to cuffing, and capture the variability in blood-flow speeds.

#### 4D in vivo imaging of haemodynamic changes in human foot vessels using PACTER

Imaging of haemodynamics in the lower extremities, specifically in the human feet, has an essential role in the diagnosis, treatment and prevention of peripheral vascular diseases and diabetes<sup>3</sup>. To evaluate the clinical applicability of PACTER, we imaged the haemodynamic changes in human foot vessels in response to vascular occlusion, which was induced by a sphygmomanometer wrapped around the participant's leg (Fig. 6a). Using PACTER, we captured 3D images of blood vessels in the instep area with single laser pulses both before and after vascular occlusion (Fig. 6b) and reconstructed the 4D dynamics of the blood vessels in response to the occlusion (Supplementary Video 12).

The maximum-amplitude projections of the 3D volumes before and after vascular occlusion (Fig. 6c) and their difference (Fig. 6d) showed that the blood vessels exhibited increased and decreased PA amplitudes, suggesting their roles as venous and arterial, respectively. As the occlusion progressed, the cuff prevented blood from leaving the foot through the veins, while blood continued to flow into the foot, causing the PA signals to increase in the veins (shown in blue in Fig. 6d). Conversely, the cuff caused a reduction in the blood volume and diameter of the arteries due to the gradual closing, leading to a decrease in the PA signals in the arteries (shown in red in Fig. 6d)<sup>58,59</sup>. This resulted in observable changes in the PA signals in the veins and arteries due to the occlusion preventing the blood from both entering and leaving the foot (Fig. 6e). After release of the cuff, the PA signals in the arteries increased, indicating the acute opening of the arteries with the full release of the blood flow, while the PA signals in the veins decreased. Even when we imaged a different instep region from the participant and inflated the sphygmomanometer at a lower rate to create vascular occlusion, similar responses from the veins and arteries were observed (Extended Data Fig. 4 and Supplementary Video 13).

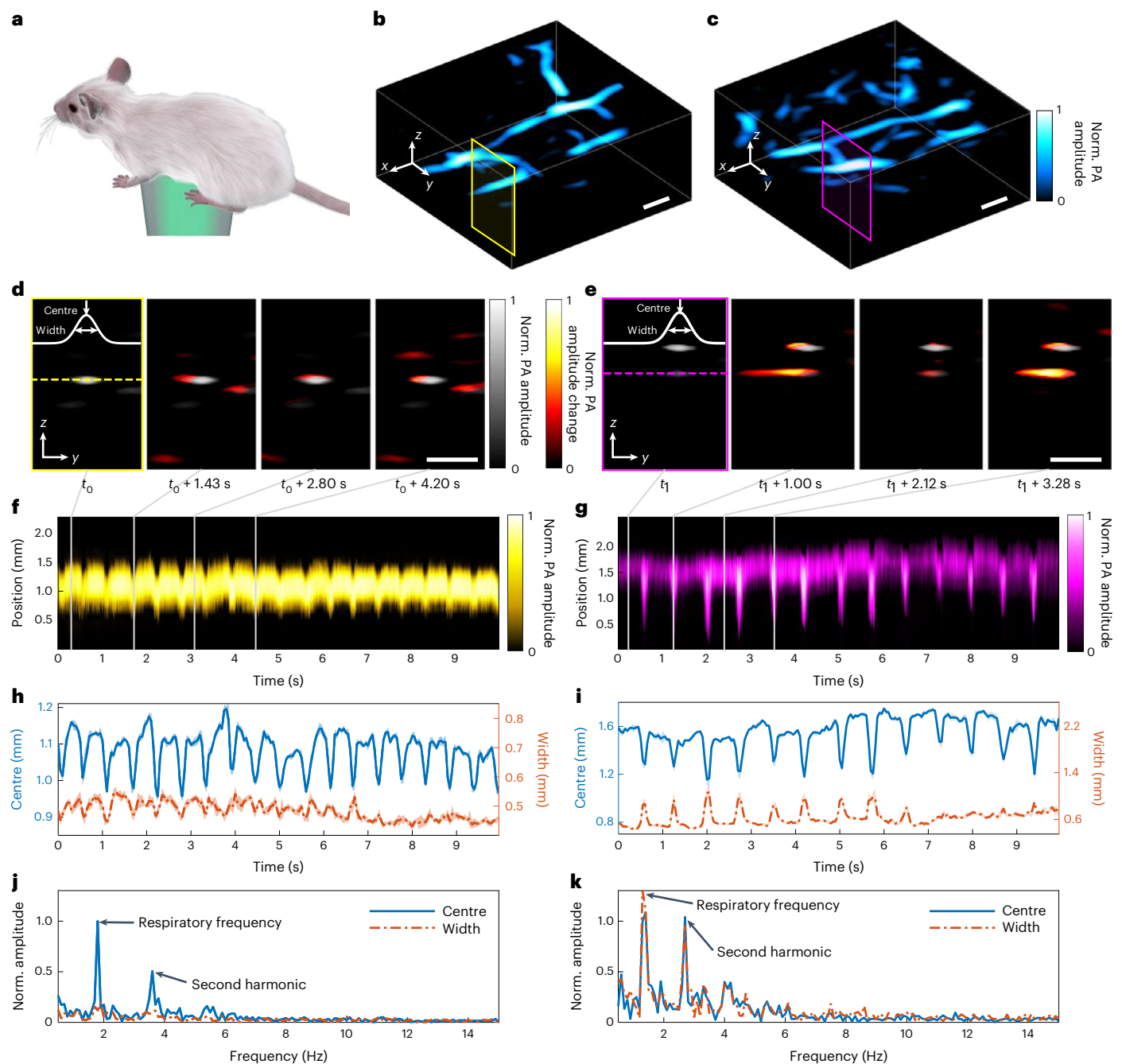


**Fig. 4 | PACTER analysis of mouse haemodynamics in vivo.** **a**, Schematic of the mouse imaging experiment. **b, c**, 3D PACTER images of the abdominal vasculature of mouse 1 (**b**) and mouse 2 (**c**). **d, e**, Cross-sectional 2D images corresponding to the yellow rectangle in **b** (**d**) and the magenta rectangle in **c** (**e**) at four different time instances from the 4D PACTER datasets.  $t_0 = 0.28$  s,  $t_1 = 0.26$  s. The white solid curves represent the Gaussian fits of the vessels' profile denoted by the yellow (**d**) and magenta (**e**) dashed lines. Differences from the first image are highlighted. **f, g**, PA amplitudes along the yellow dashed line (1D images) in **d** (**f**)

and the magenta dashed line in **e** (**g**) versus time; the time instances in **d** and **e** are indicated by vertical grey lines. **h, i**, Centre positions (blue solid curves) and widths (orange dashed curves) of the vessels versus time, based on the fits in **d** (**h**) and **e** (**i**). The shaded areas denote the standard deviations.  $n = 5$ . **j, k**, Fourier transforms of the centre positions and widths of the vessels in **h** (**j**) and **i** (**k**), showing the respiratory frequency from the vessel centre positions only (**j**) or both the vessel centre positions and widths (**k**). For **b–e**, scale bar, 1 mm.

This process, known as post-occlusive reactive hyperaemia, is consistent with previous studies<sup>58,60,61</sup>.

These results demonstrate PACTER's potential as a powerful tool for assessing vascular function in the lower extremities. The detailed and localized information that it provides could prove to be invaluable in early-stage screening, leading to more sensitive detection or early prevention of conditions such as ischaemia or ulcer development. Moreover, with its ability to accurately monitor haemodynamic

changes, PACTER could facilitate the measurement of treatment efficacy for peripheral vascular diseases and diabetes. Our technique could prove to be valuable for guiding wound treatment in vascular clinics and could facilitate post-surgical decision-making and provide longitudinal monitoring of functional wound healing. Ultimately, we believe that PACTER holds substantial promise for enhancing patient outcomes and advancing medical research in peripheral vascular diseases and diabetes.



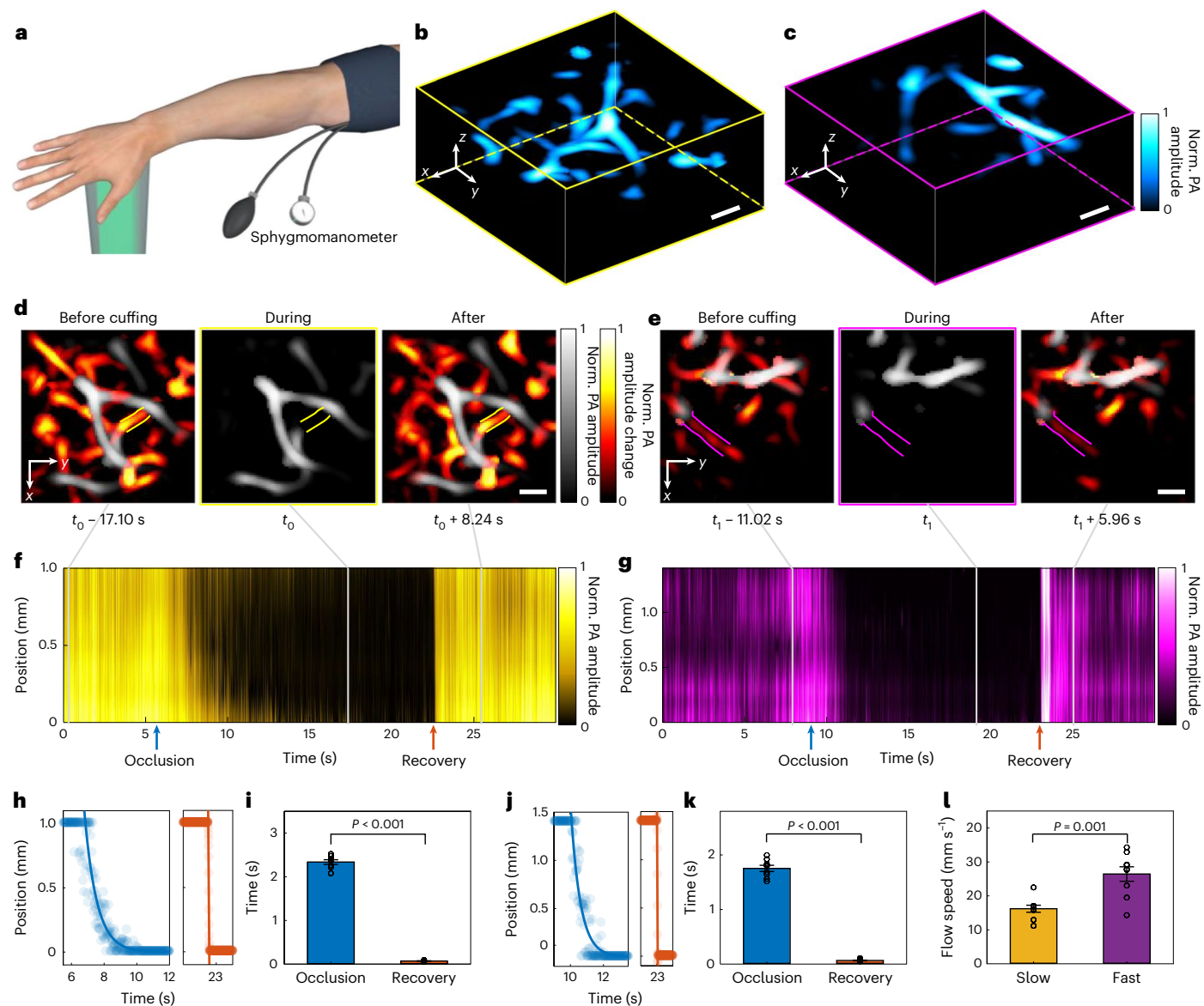


**Fig. 5 | PACTER analysis of human hand haemodynamics in vivo.** **a**, Schematic of the human hand imaging experiment. **b, c**, 3D PACTER images of the thenar vasculature of participant 1 (**b**) and participant 2 (**c**). **d, e**, Maximum-amplitude projections of the 3D volumes from the 4D PACTER datasets along the z axis in **b** (**d**) and **c** (**e**) at the time instances before, during and after cuffing.  $t_0 = 17.44$  s,  $t_1 = 19.02$  s. The solid lines flank the vessels under investigation. Differences from the images during cuffing are highlighted. **f, g**, PA amplitudes along the vessels (1D images) in **d** (**f**) and **e** (**g**) versus time; the time instances in **d** and **e** are indicated by vertical grey lines. The blue and orange arrows indicate the peak responses in the occlusion and recovery phases, respectively. **h**, The positions (solid circles) of the blood front along the blood vessel during the occlusion (left) and recovery (right) phases in **f**. The blue curve is an exponential fit with

an occlusion rate of  $1.3 \pm 0.1$  m s<sup>-1</sup>, and the orange curve is a linear fit showing a blood flow speed of  $16.1 \pm 3.1$  m s<sup>-1</sup>. **i**, Comparison between the durations of the occlusion and recovery phases in **f**. Statistical analysis was performed using a two-sample *t*-test;  $P < 0.001$ . **j**, The positions (solid circles) of the blood front along the blood vessel during the occlusion (left) and recovery (right) phases in **g**. The blue curve is an exponential fit with an occlusion rate of  $2.4 \pm 0.2$  m s<sup>-1</sup>, and the orange curve is a linear fit showing a blood flow speed of  $26.3 \pm 6.4$  m s<sup>-1</sup>. **k**, Comparison between the durations of the occlusion and recovery phases in **g**. Statistical analysis was performed using a two-sample *t*-test;  $P < 0.001$ . **l**, Comparison between the blood flow speeds during recovery in **f** and **g**. Statistical analysis was performed using a two-sample *t*-test;  $P < 0.001$ . Data are mean  $\pm$  s.e.m.  $n = 9$ . For **b–e**, scale bar, 1 mm.

## Discussion

Compared with previous techniques using ERs, including PA topography through an ER (PATER)<sup>38</sup>, PA microscopy through an ER (PAMER)<sup>39</sup> and PA imaging through a spatiotemporal encoder (PAISE)<sup>41</sup>, PACTER offers several substantial advances (Supplementary Table 1). First, previous methods allow for only 2D imaging and do not provide depth information about the object. Specifically, PAISE can generate only 2D images of thin objects, such as thin black rubber. The signals from thicker 3D objects such as in vivo blood vessels, which do not belong to the calibration data, contaminate the reconstruction. By contrast,

PACTER enables both 3D and 4D in vivo imaging in animals and humans. Second, previous techniques are not suited for long-term imaging in unstable environments. This is because PATER and PAMER are sensitive to boundary condition between the object and the ER, necessitating recalibration for different objects. Although PAISE does not require object-specific calibration, all of these techniques use post-fabrication transducers that are resin-coupled to the ERs, making them susceptible to mechanical vibrations and thermal fluctuations, therefore requiring periodic recalibration. By contrast, PACTER uses an integrated transducer that is directly fabricated onto the ER, enhancing sensitivity over



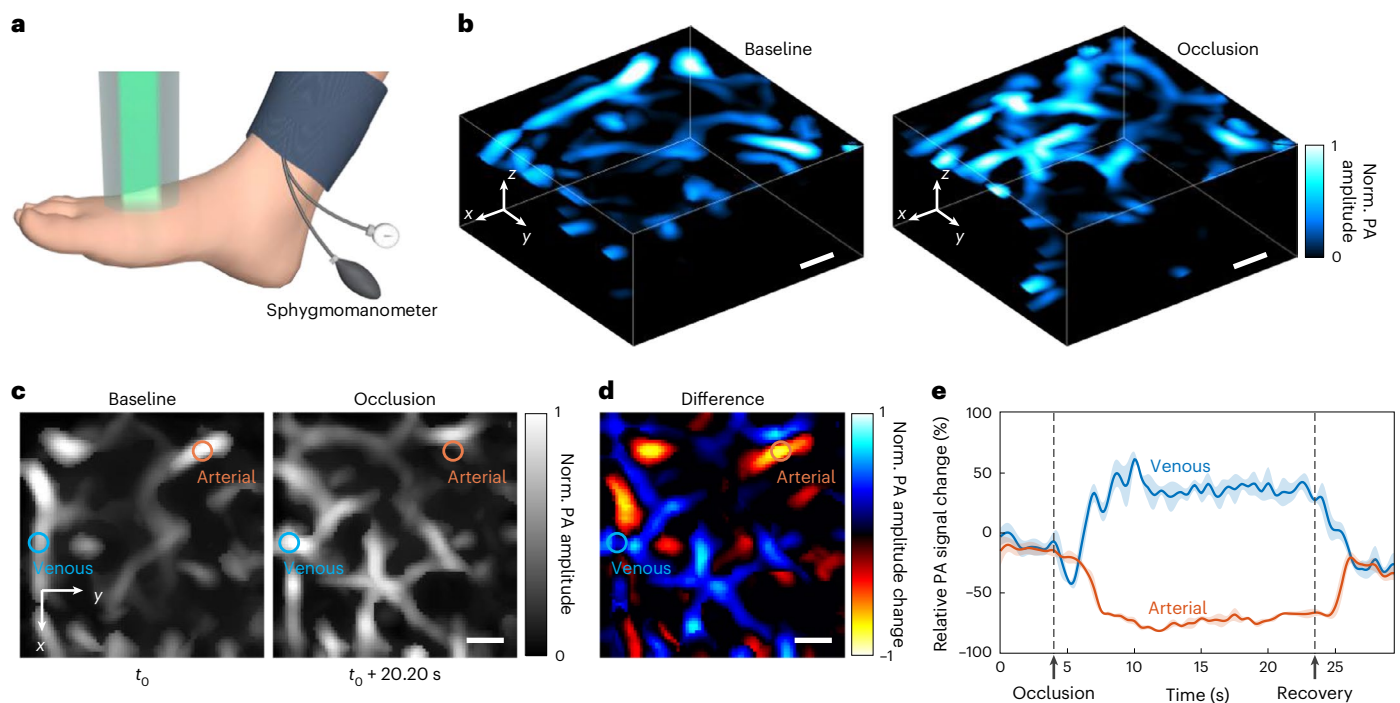


**Fig. 6 | PACTER analysis of haemodynamic changes in human foot vessels.** **a**, Schematic of the human foot imaging experiment. **b**, 3D PACTER images of the foot vessels of participant 3 before (left) and after (right) vascular occlusion. **c**, Maximum-amplitude projections of the 3D volumes from the 4D PACTER datasets along the z axis in **b**.  $t_0 = 0$  s. The blue and orange circles indicate regions

of a vein and an artery, respectively. **d**, The difference between the two images in **c**. **e**, Relative PA signals of the venous and arterial regions indicated by the blue and orange circles in **c** and **d**. The shaded areas denote the standard deviation.  $n = 5$ . The arrows and vertical lines indicate the start times of occlusion and recovery. For **b–d**, scale bar, 1 mm.

a broadband while enabling long-term in vivo imaging in unstable environments. Third, all previous works use the two-step iterative shrinkage/thresholding algorithm for reconstruction<sup>62</sup>, which can be orders of magnitude slower than the fast iterative shrinkage-thresholding algorithm (FISTA) algorithm used in PACTER<sup>63</sup>. For the substantial number of voxels ( $80 \times 80 \times 120$ ) in the 3D volumes imaged by PACTER, the reconstruction becomes computationally intensive to a prohibitive degree. Thus, without PACTER's computational innovation, which uses FISTA and temporal convolution implemented through fast Fourier transform, 3D and 4D imaging through ERs would not be possible. Finally, owing to the issues associated with previous techniques, they are unable to provide human imaging. By contrast, PACTER's ability to capture dynamic changes in vascular occlusion offers clinical potential for early detection, enhanced assessment and personalized treatment of peripheral vascular diseases.

Although the current implementation of PACTER requires motorized stages for calibration, a pulsed laser for illumination and a data acquisition card for data acquisition, these requirements could be fulfilled using cheaper and more compact alternatives. Given the system's universal calibration ability and the fact that a single calibration dataset could remain effective for at least a year (Supplementary Fig. 9), the ER in PACTER could be precalibrated, eliminating the need for motorized stages during the system's distribution. The pulsed laser and the data acquisition card could be replaced with cost-effective light-emitting diodes<sup>64</sup> and microcontrollers<sup>65</sup>, respectively, which could further enhance the portability of the system. Moreover, mass production of the ER and the single-element ultrasonic transducer could substantially lower the cost of the system, making PACTER more accessible to users or researchers in low-resource settings, further reducing the barriers to clinical translation. Furthermore, by incorporating an optical fibre, the PACTER system could be modified for handheld operation (Supplementary Fig. 17). This modification would offer increased flexibility for imaging different body parts in both animals and humans.

Owing to the large dimensions of the ER compared with the acoustic wavelength, the PA waves need to propagate a long distance inside the ER; therefore, a slight change in the speed of sound due to temperature fluctuations<sup>66</sup> would cause large differences in the measured PACTER signal (Supplementary Video 14). To address this problem, we built a temperature-stabilizing box to maintain the temperature of the ER (Supplementary Fig. 18), which stabilizes the temperature of the ER at a set temperature, for example,  $30^\circ\text{C}$ , at all times, guaranteeing a constant speed of sound throughout the experiments. Furthermore, the penetration depth of our PACTER system was limited to 3.6 mm in vivo due to the strong attenuation of 532 nm light by endogenous chromophores in biological tissue<sup>67</sup>. Changing the wavelength to 1,064 nm could increase the penetration depth to several centimeters<sup>17,22</sup>. Another limitation of PACTER is the relatively small FOV ( $8 \text{ mm} \times 8 \text{ mm}$ ) constrained by the diameter of the glass rod in the ER. We believe that the design of the ER could be further optimized to achieve a larger FOV, enabling new applications such as vascular biometrics<sup>68</sup>. Currently, the dimensions of the prism and the rod are selected on the basis of the following design considerations<sup>41</sup>: (1) the rod's diameter, which determines the FOV, should be substantially smaller than the right-angle edge length of the prism to ensure that the PA signals can be effectively scrambled; (2) the rod's length should greatly exceed the right-angle edge length of the prism to extend the duration of the object-independent signal (unaffected by the boundary condition), thereby ensuring the universal calibration capability. As shown in the simulations in Supplementary Fig. 19, once these design considerations are adhered to, minor changes in dimensions will not impact the spectra of PACTER signals, therefore maintaining the spatial resolution. Moreover, owing to the computationally intensive nature of 3D reconstruction in PACTER, the image reconstruction for a 3D volume of  $80 \times 80 \times 120$  voxels currently takes 10 min when using a CPU, which becomes a bottleneck for real-time display of the volumetric data. However, this bottleneck is anticipated

to be eliminated if the reconstruction algorithm is implemented on a GPU. Finally, the spatial resolution of PACTER is currently limited by the limited-view effect caused by the acoustic impedance mismatch between the object and the ER. This could be addressed in the future by adding an impedance-matching layer on top of the ER. Supplementary Fig. 20 illustrates three potential implementations of such an acoustic impedance-matching layer.

In summary, PACTER—a non-invasive, label-free and ultrafast imaging technique—enables 4D imaging of haemodynamics in humans using the 1D signal captured by a single detector, achieving an imaging speed of up to a thousand volumes per second. We have demonstrated PACTER's ability to visualize 4D haemodynamics in humans and small animals, particularly the haemodynamic changes in human foot vessels during vascular occlusion. We have also shown the convenience of using PACTER to image different objects, including human hands and mouse abdomens, without the need for recalibration. PACTER's high imaging speed enables immediate intervention in the case of abnormal haemodynamic changes. Moreover, PACTER's low cost and compact form factor are ideal for point-of-care testing, facilitating the quick and easy assessment of haemodynamic parameters at the bedside or in remote locations. We envision that PACTER will have an impact on a wide range of applications in biomedical research and clinical settings, including home care of diabetic-foot ulcers<sup>42</sup> or peripheral vascular diseases<sup>3</sup>, point-of-care screening for hypertension<sup>44</sup>, and simultaneous oximetry of both arterial and venous blood in intensive care units<sup>45</sup>. Furthermore, PACTER's single-shot volumetric imaging concept using a single-element detector can extend beyond optical imaging, aiding fields such as medical ultrasonography<sup>46</sup>, underwater sonar<sup>47</sup> and airborne radar<sup>48</sup>. For example, PACTER can potentially replace the transducer array for detection in ultrasonography<sup>69</sup>, thereby substantially reducing the system's cost and complexity (Supplementary Fig. 21).

## Methods

### Experimental set-up

In the PACTER system, the power of a 5 ns pulsed laser beam at 532 nm (INNOSLAB IS8II-DE, EdgeWave; 1 kHz pulse repetition rate) was controlled by a half-wave plate (WPH10M-532, Thorlabs) and a polarizing beam splitter (PBS25-532-HP, Thorlabs). The beam reflected by the PBS was sent to a beam trap (BT610, Thorlabs). The beam transmitted through the PBS was expanded by a beam expander consisting of two lenses (ACN254-050-A and AC254-100-A, Thorlabs). During calibration (Fig. 1a), the expanded beam was steered by the mirrors mounted onto two motorized linear translation stages (PLS-85, PI), which were controlled by two motor drivers (CW215, Circuit Specialists). The beam diameter was adjusted to be 2 mm by an iris (SMID12, Thorlabs), and the beam was sent through a lens (AC254-300-A, Thorlabs) and focused on top of the ER. A container with a window at its bottom sealed with an optically and ultrasonically transparent disposable polyethylene membrane was filled with bovine blood, which was used as a uniform optical absorber for calibration (Fig. 2a). The container was placed on top of the ER, where ultrasound gel (Aquasonic 100, ParkerLabs) was applied between the polyethylene membrane and the ER surface to facilitate acoustic coupling. During imaging (Fig. 1b), the beam diameter was adjusted to be 6 mm by the iris, and the beam was sent through a fly's eye homogenizer (Supplementary Note 1) consisting of two microlens arrays (64-480, Edmund Optics) and a lens (AC254-250-A, Thorlabs), which homogenized the beam in the imaging volume. Ultrasound gel was applied between the object and the top of the ER to facilitate acoustic coupling. The PACTER signals detected by the ultrasonic transducer were amplified by two low-noise amplifiers (ZKL-1R5+, Mini-Circuits), filtered by a low-pass filter (BLP-70+, Mini-Circuits), and digitized by a data acquisition card (ATS9350, AlazarTech) installed on a desktop computer. A multifunctional input/output device (PCIe-6321, National Instruments) was used to control the laser, the motorized stages and the data acquisition card.

### Universally calibratable ER

The ER in PACTER consists of a right-angle prism (PS611, Thorlabs; 25 mm right-angle edge length) and a customized optical rod (VY Optoelectronics; 18 mm diameter, 175 mm length, top and bottom surfaces polished to 60–40 surface quality). Both components were made of ultraviolet fused silica, which has good optical transparency and low acoustic attenuation. To enhance the ergodicity<sup>70</sup>, the edges of the prism were ground by a diamond saw (SYJ-150, MTI) following a sawtooth pattern to obtain chaotic boundaries<sup>40</sup>. The prism and the rod were glued by ultraviolet-curing optical adhesive (NOA68, Norland Products), after exposure under ultraviolet light for 12 h. To avoid a change in the speed of sound due to temperature fluctuations during experiments, the whole ER was sealed in a temperature-stabilizing box (Supplementary Fig. 18) regulated by a thermocouple (SA1-E, Omega Engineering), a heating pad (SRFG-303/10, Omega Engineering) and a temperature controller (Dwyer 32B-33, Cole-Parmer).

### Fabrication of the ultrasonic transducer

The fabrication process of the ultrasonic transducer is as follows. First, PMN-PT piezoelectric single crystal (CTS Corporation) was chosen as the core component for acoustic–electrical conversion due to the excellent piezoelectric coefficient and high permittivity, which is suitable for high-frequency transducers with small aperture sizes because of the general electrical impedance matching (50  $\Omega$ ). Second, on the basis of the material parameters, transducer modeling software (PiezoCAD) based on a Krimholtz–Leedom–Mataei equivalent circuit model was used to simulate and optimize the design of the transducer. Thus, a 30 MHz PMN-PT transducer with a small active aperture size of 0.4  $\times$  0.4 mm<sup>2</sup> was designed and obtained. The piezoelectric element exhibits a central frequency of 30 MHz. Third, the piezoelectric crystal was lapped to the required thickness (40  $\mu$ m), gold electrodes were sputtered onto both sides and then a layer of conductive silver paste (E-solder 3022) was deposited onto the piezoelectric sheet as a backing layer. Fourth, the acoustic stack was diced into the designed element size. Fifth, using Kapton tapes as a mask, a gold electrode was sputtered onto the corner of the hypotenuse surface of the prism of the ER (Supplementary Fig. 5). The piezoelectric element was then affixed directly to the electrode on the ER by using a thin layer of conductive silver paste. The wires were connected out to read the signals. Last, a thin parylene layer as the protective layer was deposited onto the device. As shown in Supplementary Fig. 5c, the structure of the piezo-element contains a silver matching layer, and three gold electrodes. The first and second electrodes on the both side of the PMN-PT were used for poling the PMN-PT crystal. The third electrode on the surface of the matching layer was used to connect the electrode on the prism to form the circuit as the piezo-element was connected by the double-shield coax cable. The inner conductor was connected with the E-solder conductive backing, and the copper braid was connected on the gold electrode on the prism (on the side of the piezo-element) to connect the ground side of the piezo-element.

### Data acquisition

A custom-written LabVIEW (National Instruments) program was used to trigger the pulsed laser, drive the motorized stages during calibration and acquire the data. The PACTER signals were acquired at a sampling rate of 250 megasamples per second, and a sampling length of 65,532 datapoints per acquisition. Owing to the distance between the object and the ultrasonic transducer, a 28  $\mu$ s delay was added to the data acquisition after the laser trigger. During calibration, to improve the signal-to-noise ratio of the signal, we repeated the acquisition 500 times at each calibrated virtual transducer and used the averaged signal for PACTER reconstruction. To prevent motor backlash, the data were acquired only when the motor was moving forward; the acquisition stopped when the motor returned. During imaging, to improve the

temporal resolution of the system, no signal averaging was used, and motor scanning was disabled.

### Imaging protocols

All human and animal imaging experiments were performed in accordance with relevant guidelines and regulations. The human imaging experiments followed the protocol approved by the Institutional Review Board (IRB) of the California Institute of Technology. Three healthy adult participants were recruited for this study. Written informed consent was obtained from all of the participants according to the protocol. The PACTER system was precalibrated using bovine blood, and the participants were enrolled for the imaging procedure only. For imaging the vasculature in human hands, after applying ultrasound gel, the participants were instructed to place their hands on top of the ER. For imaging the human hand haemodynamics in response to cuffing, a sphygmomanometer was wrapped around the participants' upper arm (Fig. 5a). To induce blood vessel occlusion, the sphygmomanometer was inflated to a high pressure (200 mmHg), maintained for a short time (around 15 s) and then quickly released; the total imaging time was 30 s. For imaging haemodynamic changes in human foot vessels, a sphygmomanometer was wrapped around the participant's leg (Fig. 6a). To induce vascular occlusion, the sphygmomanometer was inflated to a high pressure (200 mmHg), maintained for 15 s to 20 s, and then quickly released; the total imaging time was 30 s. The animal imaging experiments followed the protocol approved by the Institutional Animal Care and Use Committee (IACUC) of the California Institute of Technology. IRB and IACUC were aware of both protocols before approval. The fluence of the laser beam for imaging ( $5 \text{ mJ cm}^{-2}$ ) was within the American National Standards Institutes (ANSI) safety limit for laser exposure ( $20 \text{ mJ cm}^{-2}$  at  $532 \text{ nm}$ )<sup>71</sup>.

### Animal preparation

Female athymic nude mice (Hsd: Athymic Nude-Foxn1nu, Envigo; 15–20 g, aged 4–5 weeks) were used for the animal imaging experiments. Before imaging, the mouse was placed into a small chamber with 5% vaporized isoflurane mixed with air for anaesthesia induction. It was then transferred to a customized animal mount, which has a hole at the bottom such that the abdomen of the mouse can be imaged by PACTER. Ultrasound gel was applied on top of the ER, and then the animal mount was lowered until the mouse abdomen was in contact with the ER. Throughout the imaging session, the mouse was kept anaesthetized with a continuous supply of 1.5% vaporized isoflurane, its head was fixed to the stereotaxic frame of the mount and its body temperature was maintained at around  $38^\circ\text{C}$  by a heating pad.

### Sample preparation

For calibration, refrigerated lysed bovine blood (910, Quad Five) was restored to room temperature and transferred to the customized container (Fig. 2a) for acquiring the calibration signals for PACTER reconstruction. Besides bovine blood, black tape (6132-BA-10, 3M), black rubber (5508T44, McMaster-Carr) and black ink (X-1, Tamiya) were also used to test their performance as uniform optical absorbers for calibration. During the test, black tape and black rubber were cut into  $10 \text{ mm} \times 10 \text{ mm}$  sheets and placed on top of the ER, with ultrasound gel as the coupling medium; black ink was stored in the customized container. For imaging, black wires (8251T9, McMaster-Carr) were bent into curved shapes and placed into the customized container filled with water. Bar patterns were printed with black ink on a transparent film (ITF-30, Octago), cut into  $10 \text{ mm} \times 10 \text{ mm}$  sheets and placed into the water-filled customized container; a wooden stick mounted onto a manual linear translation stage (PT1, Thorlabs) was glued to the back of the film to control its  $z$  position in the imaging volume. Human hairs were embedded in a 4% agarose block (A-204-25, GoldBio), and the block was placed into the water-filled customized container during imaging. Polyurethane tubes (MRE025, Braintree Scientific;

0.012 inch inner diameter) were first placed in the water-filled customized container in straight or curved shapes, and a syringe was used to flush bovine blood through the tubes; the speed of the blood flow was controlled by a syringe pump (NE-300, New Era).

### PACTER reconstruction

In PACTER, the signal  $s(t)$  detected by the ultrasonic transducer at time  $t$  in a homogeneous medium is expressed as (Supplementary Note 3)

$$s(t) = \sum_{n=1}^N k_n(t) * \sum_{m=1}^M p_{0,m} \frac{1_{[0,\theta_1]}(\theta_{m,n}) \cos \theta_{m,n}}{\|\mathbf{r}'_m - \mathbf{r}_n\|} \delta(t - \frac{\|\mathbf{r}'_m - \mathbf{r}_n\|}{c}), t \geq 0. \quad (1)$$

Here,  $M$  and  $N$  are the numbers of the source points and the calibrated virtual transducers, respectively;  $k_n(t)$  is the normalized impulse response from the calibration at the  $n$ th virtual transducer;  $\mathbf{r}'_m$  and  $\mathbf{r}_n$  are the locations of the  $m$ th source point and the  $n$ th virtual transducer, respectively;  $p_{0,m}$  is a value proportional to the initial pressure at  $\mathbf{r}'_m$ ;  $\theta_{m,n}$  denotes the incidence angle satisfying  $\cos \theta_{m,n} = \frac{(\mathbf{r}'_m - \mathbf{r}_n) \cdot \mathbf{n}}{\|\mathbf{r}'_m - \mathbf{r}_n\|}$  with  $\mathbf{n}$  being the normal vector of the calibration plane;  $\theta_1$  is the critical angle the ultrasonic refraction from water to fused silica;  $1_{[0,\theta_1]}$  represents the indicator function defined in supplementary equation (6);  $c$  is the speed of sound in the homogeneous medium;  $\delta(t)$  denotes the delta function. To simplify the reconstruction task, we assume that the object has a homogeneous speed of sound. However, to yield high-resolution, artifact-free PAT images, the inhomogeneities of the speed of sound in biological tissues should be taken into account<sup>72</sup>.

Discretizing equation (1), we obtain the forward model

$$\mathbf{s} = H\mathbf{p}_0, \quad (2)$$

where  $\mathbf{s}$  represents a vector of length  $L$ ,  $\mathbf{p}_0$  denotes a vector of length  $M = (M_1 M_2 M_3)$  which consists of all voxels in a 3D image of size  $M_1 \times M_2 \times M_3$ , and  $H$  is the system matrix of size  $L \times M$ . This forward model has a computational complexity of  $\max\{O(MN), O(NL \log_2[L])\}$ . To obtain an image from the signals  $\mathbf{s}$ , we invert the forward model by solving the regularized optimization problem

$$\hat{\mathbf{p}}_0 = \underset{\mathbf{p}_0 \in \mathbb{R}^M, \mathbf{p}_0 \geq 0}{\text{argmin}} \|\mathbf{H}\mathbf{p}_0 - \mathbf{s}\|^2 + \lambda \|\mathbf{p}_0\|_{\text{TV}}. \quad (3)$$

Here,  $\|\mathbf{p}_0\|_{\text{TV}}$  denotes the total variation (TV) of the 3D image corresponding to  $\mathbf{p}_0$ , and  $\lambda$  is the regularization parameter. TV regularization aids in transforming an image into a new one with piecewise smoother structures, essentially constituting a form of sparseness. Using TV regularization enables the incorporation of the piecewise smoothness of blood vessels into the iterative reconstruction, considerably stabilizing the iterations. Numerically, we solve this optimization problem through a FISTA algorithm<sup>63</sup>. We chose an iteration number of 8 for the FISTA algorithm, considering the trade-off between the reconstruction image quality and the image reconstruction time. This choice was determined through a series of experiments in which we analysed the impact of different iteration numbers on both the quality of the reconstructed image and the computational time required for reconstruction (Supplementary Fig. 22). For a 3D volume comprising  $80 \times 80 \times 120$  voxels, the image reconstruction time was approximately 600 s running on a CentOS Linux 7 system with Intel Xeon Gold 6130 CPU @ 2.10 GHz.

### Image processing

The reconstructed images were first denoised using a 3D median filter (in the 3-by-3-by-3 neighbourhood) and smoothed using a 3D Gaussian filter (with a 0.1-by-0.1-by-2 standard deviation kernel). We then applied a Hessian-matrix-based vesselness filter<sup>73</sup> to the denoised images to improve the contrast of vascular structures in 3D. The effects of these



filters are illustrated in Supplementary Fig. 23, in which both the intermediate and filtered results are shown. Finally, we added the vesselness-enhanced images (self-normalized) with a weighting factor of 0.8 back to the filtered images with a weighting factor of 0.2 and obtained the presented images. The images were rendered in 3D or 4D (time-lapse 3D) using the Imaris (Bitplane) software. The speeds of bovine blood flushing through the tube in Fig. 3 were calculated by differentiating the PA amplitudes along the tube and fitting the relationship between the travelling distance of the blood front versus time. The vessels' profiles in Fig. 4 were fitted as a Gaussian function,  $\exp(-(x - x_0)^2/w^2)$ , where the centre positions and widths of the vessels were estimated from  $x_0$  and  $2\sqrt{\ln 2}w$ , respectively. The vessels' profiles in Extended Data Fig. 1 were fitted as a two-term Gaussian function, where the centre positions and widths were estimated from the first term. The positions of the blood front along the blood vessels in Fig. 5 and Extended Data Fig. 3 were obtained through thresholding the PA amplitude profiles. Denoting the total length of the blood vessel profile as  $L_p$ , we fitted the positions of the blood front along the blood vessels during the occlusion and recovery phases with  $d_o(t) = a \exp(-v_o t/L_p)$  and  $d_r(t) = -v_r t + b$ , respectively, where  $a$  and  $b$  were constants,  $v_o$  was the occlusion rate and  $v_r$  was the blood flow speed. The durations of the occlusion and recovery phases were estimated by  $t_o = 3L_p/v_o$  and  $t_r = 0.95L_p/v_r$ , respectively, which were the time it took for the blood front to propagate 95%, that is,  $1 - \exp(-3)$ , of  $L_p$ . To determine whether the differences between  $t_o$  and  $t_r$  were significant, we applied a Welch's (unequal variances)  $t$ -test to determine the  $P$  values under the null hypothesis that the mean values of  $t_o$  are not different from those of  $t_r$ . The same  $t$ -test was also performed to determine whether the difference between the blood flow speeds in Fig. 5I was significant.

### Reporting summary

Further information on research design is available in the Nature Portfolio Reporting Summary linked to this article.

### Data availability

The data supporting the findings of this study are provided within the Article and its Supplementary Information. The raw and analysed datasets generated during the study are available for research purposes from the corresponding authors on reasonable request.

### Code availability

The reconstruction code, the system-control software and the data-collection software are proprietary and used in licensed technologies, yet they are available from the corresponding author on reasonable request.

### References

- Sanz, J. & Fayad, Z. A. Imaging of atherosclerotic cardiovascular disease. *Nature* **451**, 953–957 (2008).
- Forbes, J. M. & Cooper, M. E. Mechanisms of diabetic complications. *Physiol. Rev.* **93**, 137–188 (2013).
- Norgren, L. et al. Inter-society consensus for the management of peripheral arterial disease (TASC II). *J. Vasc. Surg.* **45**, S5–S67 (2007).
- Kadem, M. et al. Hemodynamic modeling, medical imaging, and machine learning and their applications to cardiovascular interventions. *IEEE Rev. Biomed. Eng.* **16**, 403–423 (2023).
- Davies, P. F. Hemodynamic shear stress and the endothelium in cardiovascular pathophysiology. *Nat. Clin. Pract. Cardiovasc. Med.* **6**, 16–26 (2009).
- Fox, M. D. & Raichle, M. E. Spontaneous fluctuations in brain activity observed with functional magnetic resonance imaging. *Nat. Rev. Neurosci.* **8**, 700–711 (2007).
- Maurovich-Horvat, P. et al. Comprehensive plaque assessment by coronary CT angiography. *Nat. Rev. Cardiol.* **11**, 390–402 (2014).
- Provost, J. et al. Simultaneous positron emission tomography and ultrafast ultrasound for hybrid molecular, anatomical and functional imaging. *Nat. Biomed. Eng.* **2**, 85–94 (2018).
- Fan, J. L. et al. High-speed volumetric two-photon fluorescence imaging of neurovascular dynamics. *Nat. Commun.* **11**, 6020 (2020).
- Shu, X., Beckmann, L. & Zhang, H. F. Visible-light optical coherence tomography: a review. *J. Biomed. Opt.* **22**, 121707 (2017).
- Wang, C. et al. Continuous monitoring of deep-tissue haemodynamics with stretchable ultrasonic phased arrays. *Nat. Biomed. Eng.* **5**, 749–758 (2021).
- Hu, H. et al. A wearable cardiac ultrasound imager. *Nature* **613**, 667–675 (2023).
- Wang, L. V. & Hu, S. Photoacoustic tomography: in vivo imaging from organelles to organs. *Science* **335**, 1458–1462 (2012).
- Wang, L. V. & Yao, J. A practical guide to photoacoustic tomography in the life sciences. *Nat. Methods* **13**, 627–638 (2016).
- Weber, J., Beard, P. C. & Bohndiek, S. E. Contrast agents for molecular photoacoustic imaging. *Nat. Methods* **13**, 639–650 (2016).
- Zhang, H. F., Maslov, K. & Wang, L. V. In vivo imaging of subcutaneous structures using functional photoacoustic microscopy. *Nat. Protoc.* **2**, 797–804 (2007).
- Li, L. et al. Single-impulse panoramic photoacoustic computed tomography of small-animal whole-body dynamics at high spatiotemporal resolution. *Nat. Biomed. Eng.* **1**, 0071 (2017).
- Xu, M. & Wang, L. V. Universal back-projection algorithm for photoacoustic computed tomography. *Phys. Rev. E* **71**, 016706 (2005).
- Yao, J. et al. High-speed label-free functional photoacoustic microscopy of mouse brain in action. *Nat. Methods* **12**, 407–410 (2015).
- Cao, R. et al. Label-free intraoperative histology of bone tissue via deep-learning-assisted ultraviolet photoacoustic microscopy. *Nat. Biomed. Eng.* **7**, 124–134 (2022).
- Shi, J. et al. High-resolution, high-contrast mid-infrared imaging of fresh biological samples with ultraviolet-localized photoacoustic microscopy. *Nat. Photon.* **13**, 609–615 (2019).
- Lin, L. et al. Single-breath-hold photoacoustic computed tomography of the breast. *Nat. Commun.* **9**, 2352 (2018).
- Na, S. et al. Massively parallel functional photoacoustic computed tomography of the human brain. *Nat. Biomed. Eng.* **6**, 584–592 (2022).
- Özbek, A., Deán-Ben, X. L. & Razansky, D. Optoacoustic imaging at kilohertz volumetric frame rates. *Optica* **5**, 857–863 (2018).
- Wiskin, J. et al. Full wave 3D inverse scattering transmission ultrasound tomography in the presence of high contrast. *Sci. Rep.* **10**, 20166 (2020).
- Duarte, M. F. et al. Single-pixel imaging via compressive sampling. *IEEE Signal Process. Mag.* **25**, 83–91 (2008).
- Sun, B. et al. 3D computational imaging with single-pixel detectors. *Science* **340**, 844–847 (2013).
- Sun, M.-J. et al. Single-pixel three-dimensional imaging with time-based depth resolution. *Nat. Commun.* **7**, 12010 (2016).
- Stellinga, D. et al. Time-of-flight 3D imaging through multimode optical fibers. *Science* **374**, 1395–1399 (2021).
- Kruizinga, P. et al. Compressive 3D ultrasound imaging using a single sensor. *Sci. Adv.* **3**, e1701423 (2017).
- Luis Deán-Ben, X. & Razansky, D. Localization optoacoustic tomography. *Light Sci. Appl.* **7**, 18004 (2018).
- Deán-Ben, X. L., Özbek, A., López-Schier, H. & Razansky, D. Acoustic scattering mediated single detector optoacoustic tomography. *Phys. Rev. Lett.* **123**, 174301 (2019).

33. Hahamovich, E. et al. Single-detector 3D optoacoustic tomography via coded spatial acoustic modulation. *Commun. Eng.* **1**, 25 (2022).
34. Montaldo, G., Palacio, D., Tanter, M. & Fink, M. Time reversal kaleidoscope: a smart transducer for three-dimensional ultrasonic imaging. *Appl. Phys. Lett.* **84**, 3879–3881 (2004).
35. Montaldo, G., Palacio, D., Tanter, M. & Fink, M. Building three-dimensional images using a time-reversal chaotic cavity. *IEEE Trans. Ultrason. Ferroelectr. Freq. Control* **52**, 1489–1497 (2005).
36. Cox, B. T. & Beard, P. C. Photoacoustic tomography with a single detector in a reverberant cavity. *J. Acoust. Soc. Am.* **125**, 1426–1436 (2009).
37. Brown, M. D. et al. Reverberant cavity photoacoustic imaging. *Optica* **6**, 821–822 (2019).
38. Li, Y. et al. Snapshot photoacoustic topography through an ergodic relay for high-throughput imaging of optical absorption. *Nat. Photonics* **14**, 164–170 (2020).
39. Li, Y. et al. Multifocal photoacoustic microscopy using a single-element ultrasonic transducer through an ergodic relay. *Light Sci. Appl.* **9**, 135 (2020).
40. Li, L., Li, Y., Zhang, Y. & Wang, L. V. Snapshot photoacoustic topography through an ergodic relay of optical absorption in vivo. *Nat. Protoc.* **14**, 164–170 (2021).
41. Zhao, Y. & Wang, L. V. Single-shot photoacoustic imaging with single-element transducer through a spatiotemporal encoder. *J. Biomed. Opt.* **28**, 046004 (2023).
42. Andersen, C. A. Noninvasive assessment of lower extremity hemodynamics in individuals with diabetes mellitus. *J. Vasc. Surg.* **52**, 76S–80S (2010).
43. Sobieszczyk, P. & Beckman, J. Carotid artery disease. *Circulation* **114**, e244–e247 (2006).
44. Vashist, S. K. et al. Emerging technologies for next-generation point-of-care testing. *Trends Biotechnol.* **33**, 692–705 (2015).
45. Marik, P. E. & Baram, M. Noninvasive hemodynamic monitoring in the intensive care unit. *Crit. Care Clin.* **23**, 383–400 (2007).
46. Moore, C. L. & Copel, J. A. Point-of-care ultrasonography. *N. Engl. J. Med.* **364**, 749–757 (2011).
47. Trucco, A., Palmese, M. & Repetto, S. Devising an affordable sonar system for underwater 3-D vision. *IEEE Trans. Instrum. Meas.* **57**, 2348–2354 (2008).
48. Reigber, A. et al. Very-high-resolution airborne synthetic aperture radar imaging: signal processing and applications. *Proc. IEEE* **101**, 759–783 (2013).
49. Bernstein, E. F. Laser treatment of tattoos. *Clin. Dermatol.* **24**, 43–55 (2006).
50. Zhou, Q., Lau, S., Wu, D. & Kirk Shung, K. Piezoelectric films for high frequency ultrasonic transducers in biomedical applications. *Prog. Mater. Sci.* **56**, 139–174 (2011).
51. Zhou, Q. et al. Piezoelectric single crystal ultrasonic transducers for biomedical applications. *Prog. Mater. Sci.* **66**, 87–111 (2014).
52. Zhou, Q. et al. PMN-PT single crystal, high-frequency ultrasonic needle transducers for pulsed-wave Doppler application. *IEEE Trans. Ultrason. Ferroelectr. Freq. Control* **54**, 668–675 (2007).
53. Pugsley, M. K. & Tabrizchi, R. The vascular system: an overview of structure and function. *J. Pharmacol. Toxicol. Methods* **44**, 333–340 (2000).
54. Langham, M. C. et al. Evaluation of cuff-induced ischemia in the lower extremity by magnetic resonance oximetry. *J. Am. Coll. Cardiol.* **55**, 598–606 (2010).
55. Loenneke, J. P. et al. Effect of cuff type on arterial occlusion. *Clin. Physiol. Funct. Imaging* **33**, 325–327 (2013).
56. Zhou, Y., Liang, J. & Wang, L. V. Cuffing-based photoacoustic flowmetry in humans in the optical diffusive regime. *J. Biophoton.* **9**, 208–212 (2016).
57. Sinex, J. E. Pulse oximetry: principles and limitations. *Am. J. Emerg. Med.* **17**, 59–66 (1999).
58. Yang, J. et al. Photoacoustic assessment of hemodynamic changes in foot vessels. *J. Biophoton.* **12**, e201900004 (2019).
59. Choi, W. et al. Three-dimensional multistructural quantitative photoacoustic and US imaging of human feet in vivo. *Radiology* **303**, 467–473 (2022).
60. Kragelj, R. et al. Parameters of postocclusive reactive hyperemia measured by near infrared spectroscopy in patients with peripheral vascular disease and in healthy volunteers. *Ann. Biomed. Eng.* **29**, 311–320 (2001).
61. de Mul, F. F. M., Morales, F., Smit, A. J. & Graaff, R. A model for post-occlusive reactive hyperemia as measured with laser-Doppler perfusion monitoring. *IEEE Trans. Biomed. Eng.* **52**, 184–190 (2005).
62. Bioucas-Dias, J. M. & Figueiredo, M. A. T. A new TwIST: two-step iterative shrinkage/thresholding algorithms for image restoration. *IEEE Trans. Image Process.* **16**, 2992–3004 (2007).
63. Beck, A. & Teboulle, M. A fast iterative shrinkage-thresholding algorithm for linear inverse problems. *SIAM J. Imaging Sci.* **2**, 183–202 (2009).
64. Zhu, Y. et al. Light emitting diodes based photoacoustic imaging and potential clinical applications. *Sci. Rep.* **8**, 9885 (2018).
65. Fatima, A. et al. Review of cost reduction methods in photoacoustic computed tomography. *Photoacoustics* **15**, 100137 (2019).
66. Ide, J. M. The velocity of sound in rocks and glasses as a function of temperature. *J. Geol.* **45**, 689–716 (1937).
67. Yao, J. & Wang, L. V. Photoacoustic microscopy: photoacoustic microscopy. *Laser Photon. Rev.* **7**, 758–778 (2013).
68. Wang, Y. et al. A robust and secure palm vessel biometric sensing system based on photoacoustics. *IEEE Sens. J.* **18**, 5993–6000 (2018).
69. Garrett, D. C., Xu, J., Ku, G. & Wang, L. V. Whole-body human ultrasound tomography. Preprint at <https://doi.org/10.48550/arXiv.2307.00110> (2023).
70. Fink, M. & de Rosny, J. Time-reversed acoustics in random media and in chaotic cavities. *Nonlinearity* **15**, R1–R18 (2002).
71. *ANSI Z136.3-2018 American National Standard for Safe Use of Lasers in Health Care* (American National Standards Institute, 2018).
72. Jose, J. et al. Speed-of-sound compensated photoacoustic tomography for accurate imaging. *Med. Phys.* **39**, 7262–7271 (2012).
73. Jerman, T., Pernuš, F., Likar, B. & Špiclin, Ž. Beyond Frangi: an improved multiscale vesselness filter. In *Proc. SPIE Medical Imaging* (eds Ourselin, S. & Styner, M. A.) 94132A (SPIE, 2015); <https://doi.org/10.1117/12.2081147>

## Acknowledgements

We thank Y. Zhao for contributing to the universal calibration. This work was supported in part by National Institutes of Health grants R01 EBO28277, U01 EBO29823 and R35 CA220436 (Outstanding Investigator Award). The computations presented here were conducted at the Resnick High Performance Computing Center, a facility supported by the Resnick Sustainability Institute at the California Institute of Technology.

## Author contributions

Y. Zhang and L.V.W. conceived and designed the study. Y. Zhang, L.L., R.C. and K.M. built the imaging system. Y. Zhang developed the data acquisition program. P.H. developed the 3D reconstruction algorithm. Y. Zhang, L.L., R.C. and A.K. performed the experiments. Y. Zhang, P.H. and X.T. processed and analysed the data. Y. Zeng, L.J. and Q.Z. fabricated the ultrasonic transducer. L.V.W. supervised the study. All of the authors contributed to writing the paper.

## Competing interests

L.V.W. has a financial interest in Microphotoacoustics, CalPACT and Union Photoacoustic Technologies. These companies did not provide support for this work. K.M. has a financial interest in Microphotoacoustics. All other authors declare no competing interests.

## Additional information

**Extended data** is available for this paper at <https://doi.org/10.1038/s41551-023-01149-4>.

**Supplementary information** The online version contains supplementary material available at <https://doi.org/10.1038/s41551-023-01149-4>.

**Correspondence and requests for materials** should be addressed to Lihong V. Wang.

**Peer review information** *Nature Biomedical Engineering* thanks Xose Luis Dean-Ben, Wenfeng Xia and the other, anonymous,

reviewer(s) for their contribution to the peer review of this work. Peer reviewer reports are available.

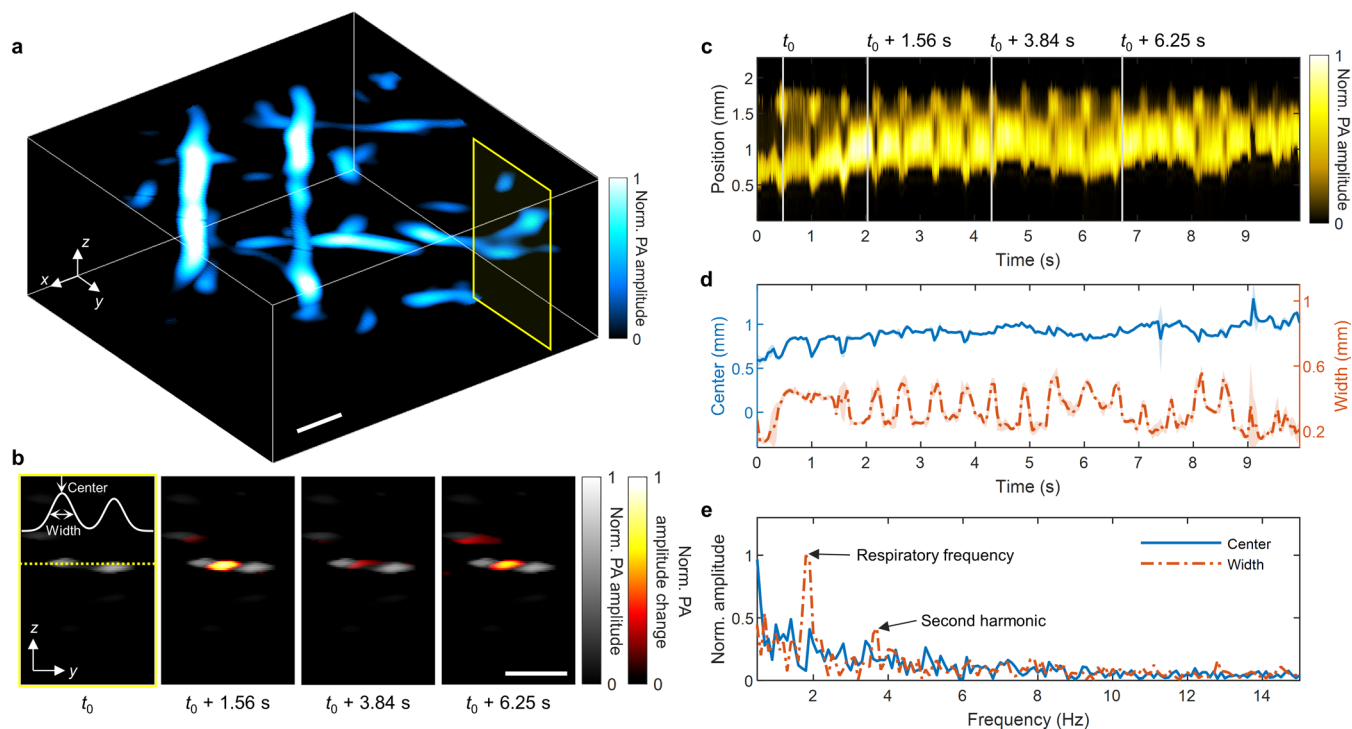
**Reprints and permissions information** is available at [www.nature.com/reprints](http://www.nature.com/reprints).

**Publisher's note** Springer Nature remains neutral with regard to jurisdictional claims in published maps and institutional affiliations.

Springer Nature or its licensor (e.g. a society or other partner) holds exclusive rights to this article under a publishing agreement with the author(s) or other rightsholder(s); author self-archiving of the accepted manuscript version of this article is solely governed by the terms of such publishing agreement and applicable law.

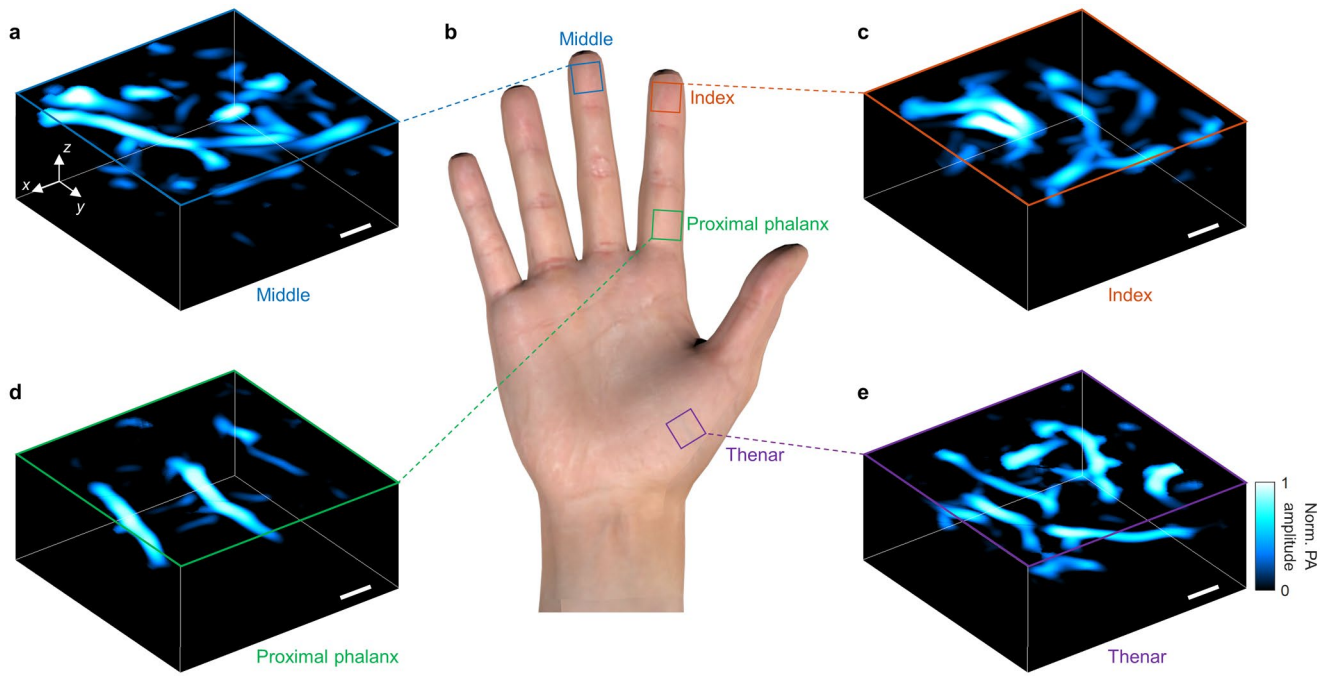
© The Author(s), under exclusive licence to Springer Nature Limited 2023



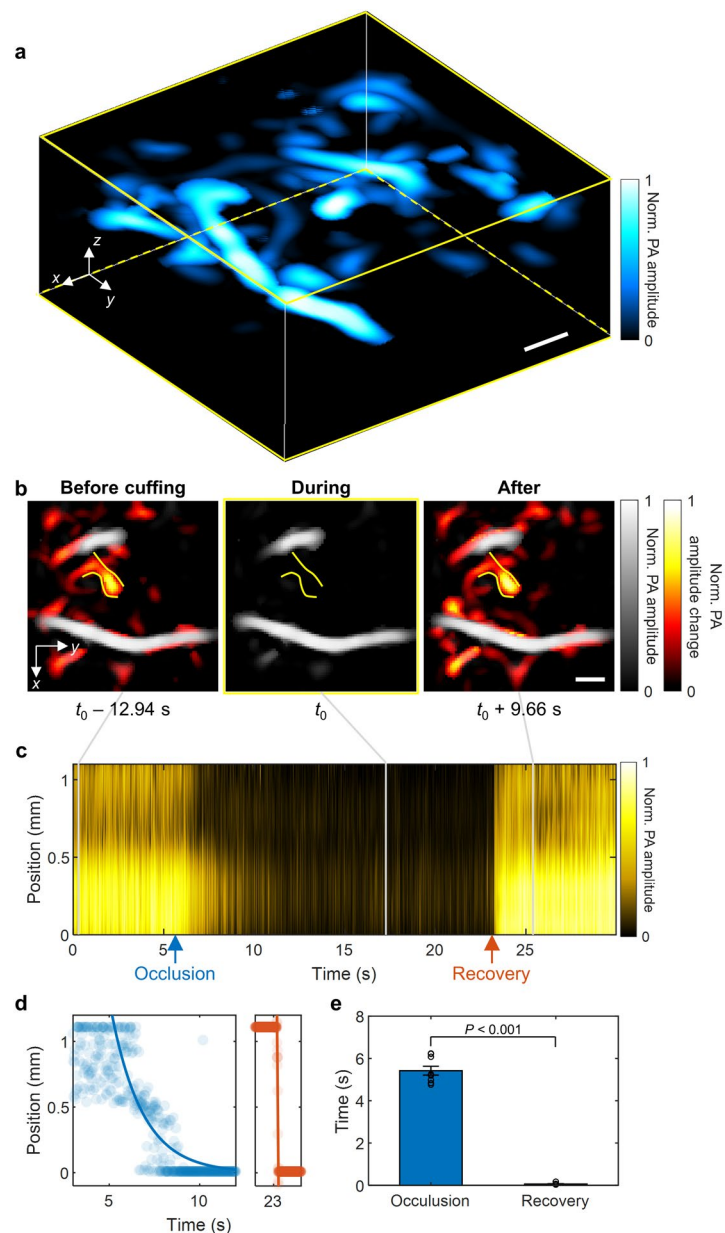


**Extended Data Fig. 1 | PACTER of mouse haemodynamics *in vivo*.** **a**, 3D PACTER image of the abdominal vasculature of mouse 3. Norm., normalized. **b**, Cross-sectional 2D images corresponding to the yellow rectangle in **a** at four different time instances from the 4D PACTER datasets.  $t_0 = 0.49$  s. The white solid curve represents a two-term Gaussian fit of the vessels' profile denoted by the yellow dashed line. Differences from the first image are highlighted in colour. **c**, PA amplitudes along the yellow dashed line (1D image) in **b** versus time, where the

time instances in **b** are labelled with vertical grey lines. **d**, Blue solid and orange dash-dotted curves represent the centre positions and widths of the vessel on the left (based on the first term of the Gaussian fit in **b**) versus time. Shaded areas denote the standard deviations ( $n = 5$ ). **e**, Fourier transforms of the centre positions and widths of the vessel in **d**, showing the respiratory frequency from the vessel widths only. Scale bars, 1 mm.



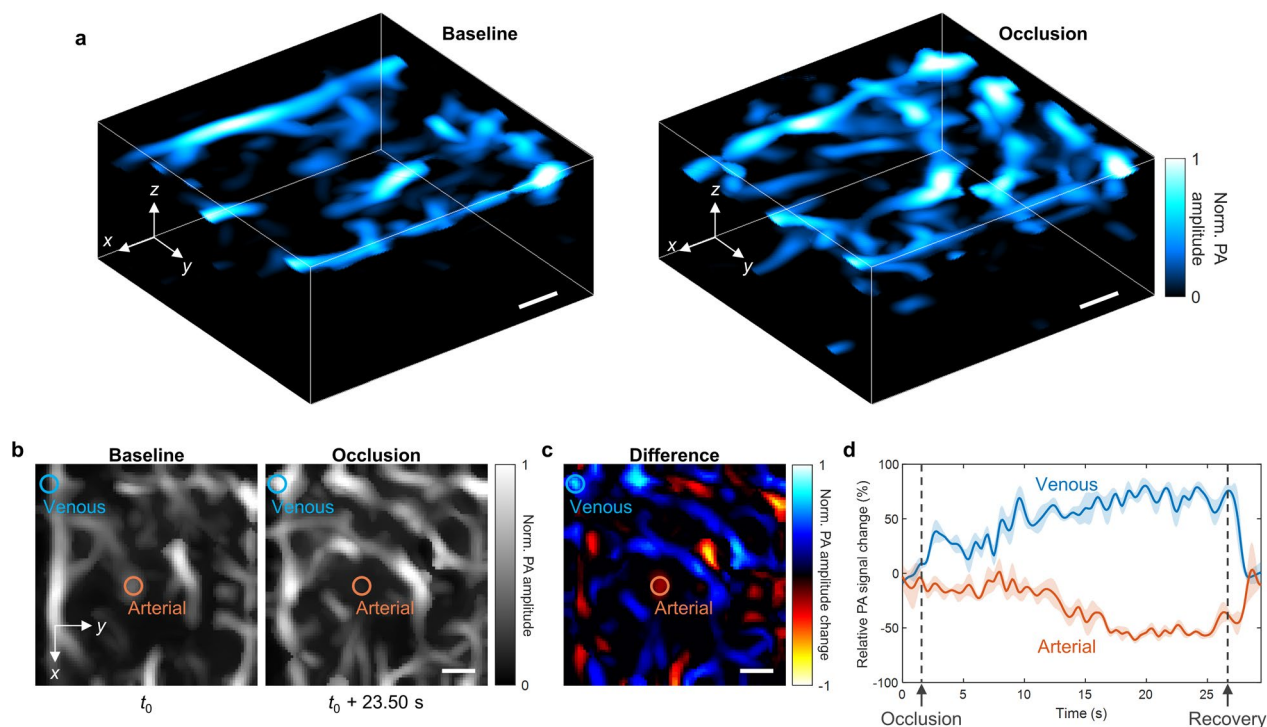
**Extended Data Fig. 2 | PACTER of human hand vasculature *in vivo*.** **a,c–e**, 3D PACTER images of the vasculature in a middle finger (**a**), an index finger (**c**), a proximal phalanx region (**d**), and a thenar region (**e**). Norm., normalized. **b**, Photograph of a human hand showing the imaged regions. Scale bars, 1 mm.



**Extended Data Fig. 3 | PACTER of human hand haemodynamics *in vivo*.** **a**, 3D PACTER image of the thenar vasculature of participant 1, in a region different from that in Fig. 5b. Norm., normalized. **b**, Maximum amplitude projections of the 3D volumes from the 4D PACTER datasets along the z axis in **a** at the time instances before, during, and after cuffing.  $t_0 = 15.34$  s. The solid lines flank the vessel under investigation. Differences from the  $t_0$  image are highlighted in colour. **c**, PA amplitudes along the vessel (1D image) in **b** versus time, where the time instances in **b** are labelled with vertical grey lines. The blue and

orange arrows indicate peak responses in the occlusion and recovery phases, respectively. **d**, Positions of the blood front along the blood vessel during the occlusion (left) and recovery (right) phases in **c**. The left blue curve is an exponential fit with an occlusion rate of  $0.6 \pm 0.1$  m/s, whereas the right orange curve is a linear fit showing the blood flow speed of  $21.6 \pm 7.9$  m/s. **e**, Comparison between the durations of the occlusion and recovery phases in **d**.  $P < 0.001$ , calculated by the two-sample *t*-test. Error bars, means  $\pm$  standard errors of the means ( $n = 9$ ). Scale bars, 1 mm.





**Extended Data Fig. 4 | PACTER of haemodynamic changes in human foot vessels.** **a**, 3D PACTER images of the foot vessels of participant 3, in a region different from that in Fig. 6b, before (left) and after (right) vascular occlusion. Norm., normalized. **b**, Maximum amplitude projections of the 3D volumes from the 4D PACTER datasets along the z axis in **a**.  $t_0 = 0$  s. The blue and orange circles

indicate regions of a vein and an artery, respectively. **c**, Difference between the two images in **b**. **d**, Relative PA signals of the venous and arterial regions indicated by the blue and orange circles in **b** and **c**. The shaded areas denote the standard deviations ( $n = 5$ ). The arrows and vertical lines indicate the start times of occlusion and recovery. Scale bars, 1 mm.

## Reporting Summary

Nature Portfolio wishes to improve the reproducibility of the work that we publish. This form provides structure for consistency and transparency in reporting. For further information on Nature Portfolio policies, see our [Editorial Policies](#) and the [Editorial Policy Checklist](#).

### Statistics

For all statistical analyses, confirm that the following items are present in the figure legend, table legend, main text, or Methods section.

n/a | Confirmed

- The exact sample size ( $n$ ) for each experimental group/condition, given as a discrete number and unit of measurement
- A statement on whether measurements were taken from distinct samples or whether the same sample was measured repeatedly
- The statistical test(s) used AND whether they are one- or two-sided  
*Only common tests should be described solely by name; describe more complex techniques in the Methods section.*
- A description of all covariates tested
- A description of any assumptions or corrections, such as tests of normality and adjustment for multiple comparisons
- A full description of the statistical parameters including central tendency (e.g. means) or other basic estimates (e.g. regression coefficient) AND variation (e.g. standard deviation) or associated estimates of uncertainty (e.g. confidence intervals)
- For null hypothesis testing, the test statistic (e.g.  $F$ )
- For Bayesian analysis, information on the choice of priors and Markov chain Monte Carlo settings
- For hierarchical and complex designs, identification of the appropriate level for tests and full reporting of outcomes
- Estimates of effect sizes (e.g. Cohen's  $d$ , Pearson's  $r$ ), indicating how they were calculated

*Our web collection on [statistics for biologists](#) contains articles on many of the points above.*

### Software and code

Policy information about [availability of computer code](#)

- Data collection 

LabVIEW 2018 (National Instruments) and MATLAB 2020b (MathWorks). The system-control software and the data-collection software are proprietary and used in licensed technologies, yet they are available from the corresponding author on reasonable request.
- Data analysis 

MATLAB 2020b (MathWorks) and Imaris 7.4.2 (Bitplane). The reconstruction algorithm and data-processing methods are described in detail in Methods. The reconstruction codes are proprietary and used in licensed technologies, yet they are available from the corresponding author on reasonable request.

For manuscripts utilizing custom algorithms or software that are central to the research but not yet described in published literature, software must be made available to editors and reviewers. We strongly encourage code deposition in a community repository (e.g. GitHub). See the Nature Portfolio [guidelines for submitting code & software](#) for further information.

## Data

Policy information about [availability of data](#)

All manuscripts must include a [data availability statement](#). This statement should provide the following information, where applicable:

- Accession codes, unique identifiers, or web links for publicly available datasets
- A description of any restrictions on data availability
- For clinical datasets or third party data, please ensure that the statement adheres to our [policy](#)

The data supporting the findings of this study are provided within the paper and its supplementary information. The raw and analysed datasets generated during the study are available for research purposes from the corresponding authors on reasonable request.

## Research involving human participants, their data, or biological material

Policy information about studies with [human participants or human data](#). See also policy information about [sex, gender \(identity/presentation\), and sexual orientation](#) and [race, ethnicity and racism](#).

Reporting on sex and gender	Sex and gender were not considered in the study design.
Reporting on race, ethnicity, or other socially relevant groupings	This study did not require the consideration of socially constructed or socially relevant categories as variables. Our protocol allowed for the recruitment of patients from all races, ethnicities and other socially relevant groups.
Population characteristics	Three healthy adult participants were recruited for this study.
Recruitment	The participants were recruited through posters. Signed informed consent forms were obtained from the participants before the study.
Ethics oversight	All the human imaging experiments followed a protocol approved by the Institutional Review Board (IRB) of the California Institute of Technology.

Note that full information on the approval of the study protocol must also be provided in the manuscript.

## Field-specific reporting

Please select the one below that is the best fit for your research. If you are not sure, read the appropriate sections before making your selection.

- Life sciences       Behavioural & social sciences       Ecological, evolutionary & environmental sciences

For a reference copy of the document with all sections, see [nature.com/documents/nr-reporting-summary-flat.pdf](https://www.nature.com/documents/nr-reporting-summary-flat.pdf)

## Life sciences study design

All studies must disclose on these points even when the disclosure is negative.

Sample size	We imaged three mice and three healthy human participants. No sample-size calculation was performed. The numbers of mice and human participants were chosen to show the applicability of the imaging technology.
Data exclusions	No imaging data were excluded.
Replication	Similar imaging results have been obtained over multiple measurements with reported sample sizes. The sample was imaged multiple times during each experiment. All replication attempts were successful.
Randomization	The experiments were not randomized. Randomization was not relevant to the study because we did not compare between samples.
Blinding	Blinding was not applicable during the experiments and during outcome assessments because we did not compare between samples or populations.

## Reporting for specific materials, systems and methods

We require information from authors about some types of materials, experimental systems and methods used in many studies. Here, indicate whether each material, system or method listed is relevant to your study. If you are not sure if a list item applies to your research, read the appropriate section before selecting a response.

## Materials &amp; experimental systems

n/a	Involvement	Included in study
<input checked="" type="checkbox"/>	<input type="checkbox"/>	Antibodies
<input checked="" type="checkbox"/>	<input type="checkbox"/>	Eukaryotic cell lines
<input checked="" type="checkbox"/>	<input type="checkbox"/>	Palaeontology and archaeology
<input type="checkbox"/>	<input checked="" type="checkbox"/>	Animals and other organisms
<input checked="" type="checkbox"/>	<input type="checkbox"/>	Clinical data
<input checked="" type="checkbox"/>	<input type="checkbox"/>	Dual use research of concern
<input checked="" type="checkbox"/>	<input type="checkbox"/>	Plants

## Methods

n/a	Involvement	Included in study
<input checked="" type="checkbox"/>	<input type="checkbox"/>	ChIP-seq
<input checked="" type="checkbox"/>	<input type="checkbox"/>	Flow cytometry
<input checked="" type="checkbox"/>	<input type="checkbox"/>	MRI-based neuroimaging

## Animals and other research organisms

Policy information about [studies involving animals](#); [ARRIVE guidelines](#) recommended for reporting animal research, and [Sex and Gender in Research](#)

Laboratory animals	Female athymic nude mice (Hsd: Athymic Nude-Foxn1nu, Envigo; 15–20 g and 4–5 weeks old).
Wild animals	The study did not involve wild animals.
Reporting on sex	Sex was not considered in the study design.
Field-collected samples	The study did not involve samples collected from the field.
Ethics oversight	All the animal experiments followed a protocol approved by the Institutional Animal Care and Use Committee (IACUC) of the California Institute of Technology.

Note that full information on the approval of the study protocol must also be provided in the manuscript.